REVISION 2

Title: Sulfur speciation in dacitic melts using X-ray absorption near-edge structure spectroscopy of the S *K*-edge (S-XANES): Consideration of radiation-induced changes and the implications for sulfur in natural arc systems

Word count: 9,922

Authors: Jackie M. Kleinsasser[1], Brian A. Konecke[2], Adam C. Simon[1], Paul Northrup[3], Antonio Lanzirotti[4], Matthew Newville[4], Camelia Borca[5], Thomas Huthwelker[5], Francois Holtz[6]

[1] *Department of Earth and Environmental Sciences, University of Michigan, Ann Arbor, Michigan*
[2] *Fathom Geophysics, LLC*
[3] *Stony Brook University, Stony Brook, New York*
[4] *University of Chicago, Argonne National Lab, Lemont, Illinois*
[5] *Swiss Light Source, Paul Scherrer Institute, Villigen, Switzerland*
[6] *Institut für Mineralogie, Leibniz Universität, Hannover, Germany*

Keywords: Sulfur, S-XANES, oxidation states, sulfate, sulfide, beam damage

ABSTRACT

The synchrotron technique of micro X-ray absorption near-edge structure spectroscopy at the sulfur *K*-edge (S-XANES) provides a unique opportunity to measure the proportion of different oxidation states of sulfur (S) in silicate glasses. Although applied extensively in the analysis of basaltic silicate glasses, few S-XANES studies have investigated variations in S oxidation states with fO_2 in felsic silicate glasses. In addition, no study has systematically compared the S-XANES results obtained from the same samples at different photon flux densities to quantify the relationship between exposure time and changes in S speciation in silicate glass, as has been done for Fe and V. This study evaluates observed differences in S speciation measured in experimentally produced H_2O-saturated dacitic glasses over a range of reducing to oxidizing conditions (from $\log fO_2 = \Delta FMQ-0.7$ to $\Delta FMQ+3.3$; FMQ is the fayalite-magnetite-quartz mineral redox buffer) and equilibrated at 1000°C and 300 MPa.

S-XANES spectra were collected at three different photon flux densities using three microspectroscopy beamlines. As is observed in S-XANES analyses of basaltic silicate glasses, beam-induced changes to the $S^{6+}/\Sigma S$ are observed as a function of photon flux density and beam exposure time. Our results demonstrate that silicate glasses of dacitic composition undergo beam-induced photo-reduction in samples equilibrated at $\Delta FMQ > +1.75$ and photo-oxidation if equilibrated at $\Delta FMQ < +1$. The time required to observe beam-induced changes in the spectra varies as a function of flux density, and our study establishes an upper photon density limit at ~1.0×10^{12} photons/μm^2. The $S^{6+}/\Sigma S$ calculated from spectra collected below this absorbed photon limit at intermediate flux densities (~$1–4 \times 10^9$ photons/sec per μm^2) are affected by beam damage, as no conditions were found to be completely free of beam-induced changes. However, the $S^{6+}/\Sigma S$ ratios calculated below the limit at intermediate flux densities are consistent with thermodynamic constraints, demonstrating that $S^{6+}/\Sigma S$ ratios calculated from S-XANES spectra can be considered reliable for estimating the oxygen fugacity.

Our results carry important implications for the S budget of felsic magmas and dissolution mechanisms in evolved melts. While our results from all three flux densities show the presence of S^{4+} dissolved in relatively oxidized ($\Delta FMQ > +1.75$) dacitic glass, even in the spectra exposed to the lowest photon densities, we are unable to rule out the possibility that the S^{4+} signal is the result of instantaneous X-ray irradiation induced beam damage using S-XANES alone. When our spectra are compared to S-XANES spectra from basaltic silicate glasses, important differences exist in the solubility of S^{2-} and S^{6+} between dacitic silicate melts, pointing to differences in solubility mechanisms as melt composition changes. This study highlights the need for further investigation into beam damage systematics, presence of S^{4+}, and the solubility mechanisms of different oxidation states of S as silicate melt composition changes.

INTRODUCTION

Understanding the solubility of sulfide (S^{2-}), sulfite (S^{4+}), and sulfate (S^{6+}) in silicate melts has remained a challenge to geochemists despite more than half a century of study. The complicated dependence of dissolution mechanisms on temperature, pressure, oxygen fugacity (fO_2), melt composition, and volatile content is compounded by difficulties in quantifying the multiple oxidation states of sulfur (S) in quenched silicate melts (glasses). The advent of utilizing X-ray absorption spectroscopy (XAS) to measure the proportions of multiple oxidation states of S present in non-crystalline silicate glasses was first presented by Paris et al. (2001). A non-destructive technique that offers high resolution and low detection limits (< 0.005 wt% S; Klimm et al., 2012), micro X-ray absorption near-edge structure spectroscopy conducted at the S *K*-edge (S-XANES) has since proven useful in determining the oxidation states and chemical environment of S in natural and synthetic silicate glasses due to the correlation between peak intensity and concentration (Li et al., 1995; Fleet et al. 2005). Multiple S-XANES studies have confirmed that S^{2-} and S^{6+} are the dominant oxidation states of S dissolved in a variety of compositions of silicate glasses (Paris et al., 2001; Bonnin-Mosbah et al., 2002; Metrich et al., 2002; 2009; Fleet 2005; Jugo et al. 2010; Lerner et al., 2021); however, the existence of S^{4+} as a stable species soluble in silicate melts remains controversial. In the earliest studies, Paris et al. (2001) and Fleet et al. (2005) did not observe any spectral evidence for the presence of S^{4+} in their synthetic basaltic to dacitic glasses, while the natural basaltic olivine-hosted melt inclusions analyzed by Bonnin-Mosbah et al. (2002) and Metrich et al. (2002) did show evidence for the presence of S^{4+}. Backnaes et al. (2008) investigated the dissolution mechanisms of S^{4+} in Na-rich glasses (14–22.8 wt% Na) and reported no clear evidence for S^{4+}.

This is the peer-reviewed, final accepted version for American Mineralogist, published by the Mineralogical Society of America.
The published version is subject to change. Cite as Authors (Year) Title. American Mineralogist, in press.
DOI: https://doi.org/10.2138/am-2022-8833. http://www.minsocam.org/

To investigate the possible stability of S^{4+} in silicate melt, Wilke et al. (2008) analyzed five silicate glasses (two of basaltic and three of andesitic composition) at the European Synchrotron Radiation Facility (ESRF; beamline ID21) in Grenoble, France, and one hydrous soda-lime silicate glass at the Swiss Light Source (LUCIA beamline) in Villigen, Switzerland. Experimental conditions ranged from 200–1000 MPa and 1000–1300°C. Those authors concluded that the presence of a S^{4+} peak in S-XANES spectra from silicate glasses is an analytical artifact caused by irradiation with an electron beam (during prior EPMA analysis) or an intense focused X-ray beam (during synchrotron S-XANES analysis). As the first study to systematically investigate beam damage in silicate glasses during S-XANES analyses, a focused beam of < 1μm induced the photo-reduction of S^{6+} to S^{4+} with increased beam intensity and time of exposure at the ESRF and the photo-oxidation of S^{2-} to S^{4+} in the soda-lime silicate glass at the SLS (Wilke et al., 2008). Wilke et al. (2008) found that beam damage is accelerated when the silicate glass contains H_2O and concluded that S^{2-} and S^{6+} are the only oxidation states of S present in silicate glasses and that S^{4+} is not a stable species. Those authors reported that the observance of S^{4+} was not immediate, but on the order of minutes depending on the beam intensity and beam size, and that certain analytical protocols can be implemented to obtain reliable, unaltered measurements (e.g., polishing samples before S-XANES analyses, using a larger beam size, moving the sample during analysis). Wilke et al. (2008) noted differences in the type and magnitude of beam damage incurred in their comparison between results collected at the SLS vs. ESRF. However, since the same samples were not analyzed at both beamlines, and therefore at different flux densities and total exposures, the authors were only able to conclude that beam damage may depend on the composition of the glass analyzed and that photon-induced

oxidation or reduction is a complex process that affects the local structural environment and is different between beamlines.

Metrich et al. (2009) also investigated the speciation of S in a variety of synthetic and natural silicate glasses at 1400°C and 1–15 kbar using S-XANES analyses conducted at the ESRF beamline ID21. Focusing on basaltic to andesitic compositions, those authors concluded that S^{4+} is a stable species in their anhydrite-saturated Fe-free experimental glasses synthesized at pressures of 4–16 kbar. However, the fO_2 of their experiments was not well constrained and the authors were only able to conclude that there may be a window where S^{4+} is stable in Fe-free or Fe-poor silicate glasses around the NNO (Ni-NiO) mineral redox buffer at higher pressures (Metrich et al., 2009). Klimm et al. (2012a, 2012b) conducted a study using a soda-lime glass, a $K_2Si_4O_9$ glass, an albitic glass, and a trondhjemitic glass and tested various analytical methods (including S-XANES) to determine the oxidation states of S present. Experiments were equilibrated at 200 MPa and either 850°C or 1000°C. Those authors demonstrate that increasing the Fe content of the melt renders the glass less susceptible to beam damage during S-XANES analyses and suggest that S^{4+} is produced at the surface during beam-sample interaction. While these studies shed new light on the effect of Fe on the solubility of S^{2-} and the utility of different methods of determining the oxidation states of S, the synthetic melt compositions are much simplified from natural silicate melts. As one of the main conclusions from Klimm et al. (2012a, 2012b) is that melt composition plays a major role in the magnitude and character of beam damage, major questions remain on how S oxidation states vary in natural melt compositions, especially more felsic compositions, as a function of fO_2.

Most recently, Lerner et al. (2021) conducted a study measuring Fe- and S-XANES in natural glasses, melt inclusions, and synthetic glasses to improve identification of beam damage

and provide methods to correct for it. Those authors assumed all S^{4+} detected was an analytical artifact as proposed by Wilke et al. (2008) and their sample set consisted of mostly basaltic melt compositions: two synthetic basaltic glasses (1500 and 2000 MPa, 1300°C), three mid-ocean ridge basalts, one basaltic glass and two melt inclusions from Kilauea, and one melt inclusion from the Lassen cinder cone in the Cascades. However, their correction method is only valid for photo-reduction of S^{6+} to S^{4+}, and the effects and conditions of photo-oxidation of S^{2-} to S^{4+} or S^{6+} remain unresolved. Therefore, to fully quantify the effects of beam damage at different levels of photon flux density and understand the possible dissolution of S^{4+} in felsic silicate melts, more work is required.

We present new experimental data to further test the conclusions presented in Wilke et al. (2008) for dacitic melts across a range of fO_2 using three different photon flux densities. Our experiments were conducted using H_2O-saturated natural dacitic melts equilibrated at ΔFMQ-0.7, ΔFMQ+0, ΔFMQ+0.5, ΔFMQ+1, ΔFMQ+1.48, ΔFMQ+1.54, ΔFMQ+1.75, ΔFMQ+2.08, and ΔFMQ+3.3, at 1000°C and 300 MPa (FMQ - fayalite-magnetite-quartz mineral redox buffer). The bulk composition and experimental conditions were selected to represent an intermediate to evolved silicate melt using a natural dacite from Quizapu Volcano, Chile, as starting material (Ruprecht et al., 2012), at mid- to upper-crustal levels in an arc magmatic system across the fO_2 range where the melt changes from sulfide- to sulfate-dominant. In the first systematic study of its kind, we compare the onset and magnitude of radiation-induced S-XANES beam damage on hydrous dacitic silicate melts defined using three radiation levels. We also discuss the implications of the S species identified and the $S^{6+}/\Sigma S$ variation as a function of fO_2 for natural arc magmas.

METHODS

Experimental approach

Ten hydrous, apatite-doped (5 wt% Durango apatite) dacitic glasses were synthesized in rapid-quench internally heated pressure vessels (IHPV) at Leibniz Universität in Hannover, Germany, at 300 MPa, 1000°C, and at nine imposed oxidation states ranging from reducing to oxidizing (fO_2 from -11.42 to -7.42 bars). All experiments were run for 72 hours (±10 minutes) and contained 0.28 or 0.38 wt% S, which was sufficient to attain sulfide saturation in the more reducing experiments (ΔFMQ-0.7, ΔFMQ+0, ΔFMQ+0.5, and ΔFMQ+1, ΔFMQ+1.48, ΔFMQ+1.54) and approach or achieve sulfate saturation in the more oxidizing experiments (ΔFMQ+1.75, ΔFMQ+2.08, and ΔFMQ+3.3). Reduced S as pyrrhotite was added for experiments conducted at ΔFMQ-0.7, ΔFMQ+0, ΔFMQ+0.5, and ΔFMQ+1 in the amount of 0.75 wt% pyrrhotite (0.28 wt% S). Elemental S was added to the more oxidizing experiments at ΔFMQ+1.48, ΔFMQ+1.54, ΔFMQ+1.75, ΔFMQ+2.08 and ΔFMQ+3.3, with the intent of adding a more oxidized form of S to attain redox equilibrium faster. In these experiments 0.28 wt% S was added to the capsules run at ΔFMQ+1.75 and ΔFMQ+3.3, while 0.38 wt% S was added for those at ΔFMQ+1.48 and ΔFMQ+1.54. Two capsules were run at the same time at ΔFMQ+2.08, with 0.28 wt% and 0.38 wt% S. Furthermore, additional Fe was added to the oxidized charges as hematite (Fe_2O_3) in the same proportion as that provided by pyrrhotite in the reduced experiments (1 wt% S to 2.4 wt% hem). Table 1 gives the experimental details. In order to more closely represent a hydrous arc magma, all experiments were saturated with H_2O by the addition of ~6.75 wt% pure H_2O to the dry starting material. VolatileCalc 2.0 (Newman and Lowenstern, 2002) was used to estimate the amount of water required to reach H_2O-saturation.

For all runs except the most oxidizing (ΔFMQ+3.3), the fO_2 in the IHPV was imposed by adding calculated amounts of H_2 gas before heating along with the Ar pressure medium (see pH_2 initial, Table 1) and monitored throughout the duration of the experiment using a Shaw-membrane

(Berndt et al., 2002). Noble metal capsules are permeable to H_2 at high pressure. Thus, considering the equilibrium reaction of water formation ($H_2 + ½ O_2 \leftrightarrow H_2O$), increasing amounts of H_2 in the pressure medium results in a decrease of fO_2 in water-saturated samples. Since all experiments were volatile saturated, we assumed that $a_{H2O} = 1$, which allowed us to calculate the necessary pH_2 initial to achieve the target fO_2 (Table 1). In our experiments, the run duration was too short to attain osmotic equilibrium between the Shaw membrane and the pressure vessel (the pH_2 in the membrane was still increasing after 72 hours) so that the pH_2 prevailing in the experimental sample at high temperature could not be measured accurately with the Shaw membrane. However, the expected pH_2 was compared to the measured pH_2 values at osmotic equilibrium by Berndt et al. (2002) in a series of tests performed on the same pressure vessel that was used for this study. The difference between both values was low or even negligible and transfers to an fO_2 difference of less than 0.1 log unit (Berndt et al., 2002), which confirmed previous observations made by Scaillet et al. (1992) and agrees with more recent observations (Michaud et al., 2022). We acknowledge that the presence of additional volatile species in significant amounts would lower the a_{H2O}, which is an additional source of uncertainty in the calculated fO_2 values. However, Zajacz et al. (2012; 2013) have shown that, for intermediate silicate melts, the S concentration in aqueous fluid in equilibrium with sulfide- and anhydrite-saturated melts at similar pressures and temperatures is only on the order of 3–5 mol%. Those results, taken together with the small spread of expected values of the EPMA-derived water concentrations and the fact that the anhydrous starting glass total is very close to 100 wt%, point to the a_{H2O} being very close to 1 for these experiments, which would not affect significantly the resulting fO_2. Considering that the activity of H_2O was slightly below 1 and that pH_2 at high temperature was calculated from initial, we estimate that the

uncertainty of fO_2 is lower than ± 0.25 log units. Reported temperatures are accurate to ± 5°C and reported pressures to ± 1 MPa.

An isobaric rapid quench terminated each experiment and a small pressure increase of ~3–5 bars related to the capsule drop from the hot end to the cold bottom of the vessel confirmed the success of this technique. The recovered capsules were then cleaned with ethanol and weighed to verify capsule integrity; any capsules that showed weight loss after quenching were discarded. A total of 10 experimental run products were extracted, mounted in epoxy and polished for analysis.

The quenched glasses were first analyzed using EPMA at the University of Michigan on a CAMECA SX-100 to measure major (Si, Al, Ca, Mg, Fe, Na, K) and minor element (Ti, P, Mn, Cl, S) concentrations (Table 2). Two beam conditions were used for each analyzed spot, both with an accelerating voltage of 15 keV and beam size of 10 μm but with distinct beam currents. Silicon, Al, Ti, Ca, Mg, Fe, Mn, P, K, and Na were measured first using a beam current of 6 nA, followed by measurement of S and Cl using a beam current of 40 nA to achieve low detection limits for these latter elements (0.005 wt% for S and 0.014 wt% for Cl). See Supplementary Table S1 for EPMA details. Every attempt was made to perform analyses on crystal-free glass areas, and care was taken to monitor the contribution of other phases within the electron beam activation volume. Calcium and P were used as a proxy for apatite, and analyses with elevated concentrations of both CaO and P_2O_5 together with a decrease in Al_2O_3, K_2O, or Cl were discarded.

Assessment of equilibrium

Equilibrium was assessed by measuring the compositional homogeneity of the run product glasses and performing an additional experiment to verify that the imposed fH_2 of the vessel was equilibrated with that inside the capsule. Low standard errors for all elements measured in the

220 silicate glasses (i.e., quenched dacitic melts) as reported in Table 2 evince that the melts were
221 compositionally homogenous, given that the EPMA spot analyses were conducted across the entire
222 exposed surface of each sample. Synchrotron X-ray fluorescence maps confirmed homogeneity of
223 S as well as P, Si, Al, and Mg across the glass areas of each mapped sample. Achieving
224 homogeneity of Fe and S is especially important in this test as these elements were initially
225 mechanically mixed and added to the capsules. One additional experiment (QD-305) that
226 contained 1.5 wt% pyrrhotite as the source of 0.57 wt% S was performed under oxidizing
227 conditions (ΔFMQ+3.3) to test if the melt reached redox equilibrium within the run duration.
228 Importantly, the test resulted in the same phase assemblage as the experiment conducted at
229 ΔFMQ+3.3 (QD2-5; Table 1) that started with 0.28 wt% elemental S at ΔFMQ+3.3, indicating that
230 72 hours was sufficient to oxidize the reduced S and Fe initially present. This result is consistent
231 with previous experiments involving S under the same temperature and pressure conditions using
232 the same experimental vessels that demonstrated that redox equilibrium was reached in <10 hours
233 (Fiege et al., 2014).
234
235 **Micro X-ray absorption near-edge structure spectroscopy**
236 To measure the S oxidation states of the quenched glasses, fluorescence mode S-XANES
237 was conducted at the Advanced Photon Source (the APS) of Argonne National Laboratory,
238 Chicago, IL, USA (see Sutton et al. 2017 for beamline specifications), the Swiss Light Source
239 (the SLS; https://www.psi.ch/en/sls/phoenix.com) of the Paul Scherrer Institute, Villigen,
240 Switzerland, and the National Synchrotron Light Source-II (the NSLS-II) of Brookhaven
241 National Laboratory, Upton, NY, USA (see Northrup, 2019 for beamline specifications). Details
242 on the beamline setup parameters used for this study can be found in Table 3. All three beamlines
243 employ double crystal (silicon 111) monochromators to generate monochromatic radiation

244 focused with a Kirkpatrick-Baez mirror system. Following the protocol suggested in Wilke et al.
245 (2008), all sample surfaces were freshly polished prior to S-XANES analyses at each beamline to
246 remove any altered regions from previous EPMA or S-XANES analyses. Due to the presence of
247 apatite and other crystals in the dacitic glass, a focused microbeam was used for mapping and
248 spot XAS analyses. All samples were held stationary during XAS acquisition.

249 Freshly polished sample surfaces were positioned at 45° from the incoming beam and
250 fluorescence detectors at 90° to minimize scattering contributions. We followed the collection
251 and processing procedures described in Konecke et al. (2017) and Konecke et al. (2017; 2019).
252 X-ray fluorescence (XRF) maps were acquired at all beamlines immediately preceding spectra
253 collection to select clean areas of glass for analyses, which we acknowledge exposed the sample
254 surface to the beam prior to spectra acquisition. Table 3 documents the scan parameters used at
255 each beamline and Supplementary Figure S1 shows examples of how the XRF maps were used
256 for point selection. At the SLS and the APS beamlines S fluorescence spectra were collected
257 using energy dispersive four-element silicon drift diode detector arrays and corrected for detector
258 and electronics dead time. A single ultra-low energy Ge fluorescence detector was used at the
259 NSLS-II. Fixed analog signal processing was used at NSLS-II, Xspress3 adaptive digital signal
260 process at the APS, and the XMAP digital processing system at the SLS. The S-XANES spectra
261 were collected by scanning the incident beam energy from 2440 to 2550 eV using a slightly
262 different setup at each beamline (see Table 3). While step scanning was used at the SLS and the
263 APS, measurement at the NSLS-II which consisted of 15–100 on-the-fly-scans (e.g., quick,
264 continuous motion scans). Wilke et al. (2008) also used this method for spectra collected at
265 ESRF beamline ID21. All scans were divided into the same three energy regions: i) a pre-edge
266 background region from 2440–2460 eV, ii) the edge region from 2460–2500 eV, and iii) a post-

edge region from 2500–2550 eV. The European Synchrotron Radiation Facility S K-edge XANES spectra database was used to identify the S^{6+} (~2482 eV; anhydrite), S^{4+} (~2478 eV; sodium sulfite), and S^{2-} (~2470 eV; pyrrhotite) peak energy position for the unknowns. As noted in Table 3, the monochromator calibration for sulfate-containing standards at each beamline is slightly different, with the S^{6+} peak occurring at similar but distinct energies. This causes the peak positions of the various S species to be shifted to slightly different energies for each beamline. For this reason we shifted the energy scales in the figures so that the S^{6+} peak of all spectra was centered at 2482 eV to facilitate direct comparison of peak positions.

Three different photon flux densities were used, one at each beamline, and converted to three levels of absorbed radiation per μm^2 by calculating the product of photon flux density and data acquisition time. Casting our results in terms of the three radiation levels enables the comparison of the effects of different radiation levels on changes in the S speciation (i.e., beam damage) and allows for the results to be generalized and utilized at beamlines with different configurations, as has been done for Fe- and V-XANES (see Cottrell et al., 2018; Lanzirotti et al., 2022). The starting point for the radiation level estimates is the photon flux density (photons/second per μm^2), which is detailed for each beamline in Table 3. At the APS, the photon flux density was estimated and recorded for each measurement and can be found in the raw data files of the APS spectra in the Supplementary material. For our purposes the photon flux densities at each fO_2 were averaged for the APS points. The photon flux density for the NSLS-II and the SLS measurements were estimated to be similar across all analyses: ~2.0×10^7 photons/sec per μm^2 at the NSLS-II and 1.0–4.5×10^{10} photons/sec per μm^2 at the SLS. The flux density and absorbed radiation estimates for each point are detailed in Supplementary Table S2. Care was taken to analyze large pockets of glass that were both bubble- and crystal-free, even

below the surface as XRF has a significant sampling depth as compared to, e.g., SEM. Spectra that showed a small peak at ~2483 eV were discarded, as that peak is characteristic of an apatite S-XANES spectra (Fleet et al., 2005). S-XANES spectra were also monitored for contribution from S-bearing epoxy, which was not observed (see Fig. 1 in Konecke et al. 2019).

For data analysis, S-XANES spectra were normalized against the incident flux (I_0), the pre- and post-edge set to 0 and 1, respectively, and, if applicable, spectra from the same glass spot were merged using the XAS analysis software Athena (Ravel and Newville, 2005). For spectra collected using the fly-scan method at the NSLS-II, merged spectra were also rebinned to match the step sizes from the APS and SLS measurements and to reduce noise resulting from over-sampling in energy. Peak positions and areas were then fitted using the Fityk software version 1.3.1 (Wojdyr, 2010). First, an exponentially modified Gaussian (EMG) cumulative distribution function was fit to subtract the background. Gaussian area curves were then fit to each peak, from which the integrated $S^{6+}/\Sigma S$ peak area ratios were calculated and compared following Konecke et al. (2019). Peak area ratios calculated from different samples at the same fO_2 and incident flux were averaged to obtain the reported $S^{6+}/\Sigma S$ and standard errors. The original, raw spectra files collected at each beamline and the peak area ratios used to calculate the $S^{6+}/\Sigma S$ of all spectra included in this study are available as a zipped folder in the Supplement and in Supplementary Table S3, respectively.

RESULTS

Run products

All run products contain quenched dacite glass, apatite, a spinel-group mineral, and an exsolved volatile phase (Fig. 1). Table 1 presents the glass compositions and phase assemblages.

The glasses equilibrated at ΔFMQ-0.7, ΔFMQ+0, ΔFMQ+0.5, ΔFMQ+1, ΔFMQ+1.48, and ΔFMQ+1.54 are sulfide-saturated and contain 0.0191–0.0505 wt% S. The glasses equilibrated at ΔFMQ+1.75 and ΔFMQ+2.08 are both sulfide- and sulfate-undersaturated and contain 0.0551 and 0.0307–0.1045 wt% S, respectively, while the glass equilibrated at ΔFMQ+3.3 contains 0.1138 wt% S and reached sulfate-saturation (i.e., contains anhydrite). The main sulfur-bearing phase (if present) observed at each fO_2 is expected given the imposed redox conditions and provide evidence that redox equilibrium was attained during the 72 hour experimental duration.

Beam damage assessment

With the results of Wilke et al. (2008) in mind, we implemented two analytical protocols to monitor beam damage when analyzing the hydrous dacitic glasses: (1) collecting 2–3 spectra per point at the APS and the SLS and 1–100 spectra at the NSLS-II to monitor changes in the spectra from the first to subsequent scans, and (2) performing time scans at the SLS and the APS on fresh spots to inspect for systematic changes in S^{2-}, S^{4+}, and S^{6+} counts over time (as in Metrich et al., 2009). Due to the lower flux density and fluorescence signal for S at the NSLS-II beamline, only samples containing higher melt S contents were able to be analyzed (ΔFMQ+1.48, ΔFMQ+1.54, ΔFMQ+1.75, ΔFMQ+2.08, and ΔFMQ+3.3).

By casting the results in terms of photon flux density or absorbed radiation per μm^2, S-XANES data from different beamlines can be directly compared even though differences in the sample chamber environment, scan durations, and type of scan exist among the three beamlines used in this study (see Table 3). The data are presented in three radiation levels that were calculated from the photon flux densities. The highest radiation level was analyzed using a photon flux density of 1.0–4.5 x 10^{10} photons/sec per μm^2. A total of 7.2 x 10^{12} to 3.24 x 10^{13}

photons/μm^2 was acquired by the sample after each ~12 minute scan. The intermediate radiation level was analyzed using a photon flux density of 1.4–5.7 x 10^9 photons/sec per μm^2, corresponding to a total of 7.63 x 10^{11} to 3.07 x 10^{12} photons/μm^2 after each ~9 minute scan. The lowest radiation level was analyzed using a photon flux density of 2.0 x 10^7 photons/sec per μm^2, which corresponds to 3.15 x 10^{10} to 2.10 x 10^{11} photons/μm^2 for 15 to 100 fly-scans, respectively.

Experiments conducted at ΔFMQ+1.75 and ΔFMQ+3.3 were analyzed at all three radiation levels, so the comparison of spectra at each level enables the most direct assessment of the effects of different photon flux densities. Figure 2 presents normalized spectra of the experiments conducted at ΔFMQ+3.3 and ΔFMQ+1.75. Notations and colors are consistent for Figure 2 and subsequent figures showing spectra. The peak heights are not directly comparable between beamlines, but a semi-quantitative comparison can be made. In Figure 2a-b, the average of the first 15 fly-scans from the lowest level has the highest S^{6+} peak, the lowest S^{4+} peak, and no S^{2-} peaks. The spectra from the highest level and scan 2 from the intermediate level are very similar overall in Figure 2a-b. The general progression from the highest S^{6+} peak and lowest S^{4+} and S^{2-} peaks to the lowest S^{6+} peak and the most prominent S^{4+} and S^{2-} peaks is as follows: average of the first 15 scans from the lowest level, the average of the last 15 scans from the lowest level, scan 1 from the intermediate level, and then scan 2 of the intermediate level and all three scans from the highest level. The pattern precisely follows an increasing quantity of photons absorbed per μm^2 over time, as would be expected.

Figure 3 presents normalized spectra from the high and intermediate radiation levels for the more reduced samples at ΔFMQ-0.7, ΔFMQ+0, ΔFMQ+0.5, and ΔFMQ+1. The spectra are normalized but not merged to show multiple scans collected on the same point. One of the first

358 evident differences between the spectra collected at the highest and intermediate levels is that the
359 highest level spectra are less noisy, as a result of a higher count rate. The more jagged spectra
360 produced at the intermediate level are due to relatively lower fluorescence signal because of a
361 lower incident photon flux. The highest level spectra show some change in peak height over time
362 (Fig. 3a-b and 3g), but the magnitude is generally less than the changes observed in the
363 intermediate level spectra. The sharp S^{2-} peak at 2470.3 eV increases slightly in Fig. 3b and
364 decreases slightly in Figure 3a, 3d, and 3f. The broad S^{2-} peak at 2475.5 eV consistently shrinks
365 with subsequent scans and at both the highest and intermediate levels in Figure 3a-c, 3e-f, and
366 3h. No S^{4+} peak is detected in the more reduced spectra in Figure 3. The S^{6+} peak grows in a
367 number of spectra from both the radiation levels in Figure 3a-b and 3g-h.
368 Figure 4 shows a comparison between the normalized average of the first 20 (Fig. 4a-b)
369 or three (Fig. 4c) scans vs the average of the final 20 or three scans collected at the lowest
370 radiation level. From Figure 4 we observe the largest changes in the spectra in Figure 4b, which
371 had the highest number of fly-scans collected (94) and therefore the longest beam interaction
372 time (164.5 minutes). Figure 4c, the sample with the fewest fly-scans (15) and shortest beam
373 interaction time (26.25 minutes), shows a modest decrease in the S^{6+} peak over time, however,
374 no great change in peak heights of S^{4+} or S^{2-}. The lower S content of Figure 4a makes spectra
375 comparison difficult due to the lower signal/noise and consequent uncertainty in edge-step
376 normalization. A step scan was also tested on one experiment conducted at ΔFMQ+2.08 (QD9-4)
377 at the lowest radiation level. Each step scan took ~48 minutes to complete (5.76×10^{10}
378 photons/μm^2 per scan) and a total of 14 step scans were taken on a single point of QD9-4, the
379 same sample as in Fig. 4c. The first step scan is comparable to the sum of the first 15 fly-scans.
380 Figure 5 compares the first, second, and 14th step scan. Beam damage is noted already by the

second scan, evidenced by the growth of a broad peak centered at 2477.3 eV in the second scan and the rise of the region between 2473–2476 eV by the 14th scan. The S^{6+} peak also decreases with each subsequent scan, consistent with what is observed in Figure 2.

Figure 6 shows the results of the second beam damage assessment technique, where time scans document the intensity changes in S counts for the experiment conducted at ΔFMQ+3.3 at the intermediate and highest radiation levels at a single energy over time. Time scans are conducted at a single energy and therefore only monitor a single S oxidation state over time and are plotted as the relative fractional change in measured change intensity over time, as has been used for Fe in Cottrell et al. (2018) and for V in Lanzirotti et al. (2022). In Figure 6a, both radiation levels show an initial maximum value for S^{6+} intensity that decays and reaches a steady-state after ~60 seconds at the highest level and ~120 sec at the intermediate level. However, the rate of decay is much higher at the highest level, where an intensity change of ~40% occurs within the first ~20 seconds compared to an intensity change of ~35% over 120 seconds of analysis time at the intermediate level. In Figure 6b, contrasting behavior is observed for S^{4+} intensity. At the highest level, two separate time scans reveal the same behavior for S^{4+} as S^{6+}: a maximum value followed by a decrease of ~50% starting intensity within ~30 seconds. In the time scan from the intermediate level, the S^{4+} intensity instead increased by ~175% over time, leveling off after ~60 seconds. The time scans of the S^{2-} intensity (Fig. 6c) show mixed results. The intermediate level and one of the highest level scans show the S^{2-} intensity increasing over time without truly leveling off, with the rate of increase being higher at the intermediate level (>250% increase) compared to the highest level (~225% increase) over the total scan duration. The other time scan at the highest level shows similar behavior to the S^{6+} and S^{4+} scans, where the S^{2-} intensity decays by ~60% within the first seconds of the scan.

This is the peer-reviewed, final accepted version for American Mineralogist, published by the Mineralogical Society of America.
The published version is subject to change. Cite as Authors (Year) Title. American Mineralogist, in press.
DOI: https://doi.org/10.2138/am-2022-8833. http://www.minsocam.org/

S-XANES spectra

Figure 7 summarizes the results of S-XANES analyses from the highest radiation level for six glasses at ΔFMQ+3.3, ΔFMQ+1.75, ΔFMQ+1, ΔFMQ+0.5, ΔFMQ+0, and ΔFMQ-0.7. The spectra shown are the result of 5–7 step scan spectra from different spots that have been merged. At the highest level, the most oxidizing experiments at ΔFMQ+3.3 and ΔFMQ+1.75 both contain dominantly S^{6+}, with intense peaks at 2482 eV, but the spectra also show low-intensity humps at the positions for S^{2-} (2470 and 2475 eV) and S^{4+} (2477 eV). At intermediate fO_2 (ΔFMQ+1, ΔFMQ+0.5) the S^{6+} peak intensity of the highest radiation level spectra is greatly reduced compared to the ΔFMQ+1.75 and ΔFMQ+3.3 spectra, and is accompanied by more intense S^{2-} peaks and the disappearance of the S^{4+} peak. The spectra from the most reducing experiments at ΔFMQ+0 and ΔFMQ-0.7 are dominated by the S^{2-} peaks and have the lowest-intensity S^{6+} peak.

Figure 8 summarizes the 1st scan collected at the intermediate radiation level for nine glasses at ΔFMQ+3.3, ΔFMQ+2.08, ΔFMQ+1.75, ΔFMQ+1.54, ΔFMQ+1.48, ΔFMQ+1, ΔFMQ+0.5, ΔFMQ+0, and ΔFMQ-0.7. The spectra shown are the result of 2–5 step scan spectra from different spots that have been merged. The ΔFMQ+3.3 experiment shows exclusively S^{4+} and S^{6+}, with no evidence for S^{2-} species. Dacitic glass from the ΔFMQ+2.08 experiment (QD9-4) is dominated by S^{6+} and S^{4+}, with a minor contribution of the broad S^{2-} peak at 2475 eV. Spectra from the ΔFMQ+1.75 experiment reveal a relatively smaller peak for S^{4+} compared to the more oxidized spectra at ΔFMQ+3.3 and ΔFMQ+2.08 and the possible presence of a S^{2-} peak. Dacitic glasses at ΔFMQ+1.54 and ΔFMQ+1.48, which are at the middle of the sulfide-sulfate transition, show prominent S^{6+} and S^{2-} peaks (both sharp and broad S^{2-}) and only a minor S^{4+} peak that is discernable from the broad S^{2-} peak. Spectra for the more reduced glasses are

similar to spectra collected at the highest radiation level, with an abrupt decrease in the S^{6+} peak starting at ΔFMQ+1 and then a gradual decrease in S^{6+} peak height with a decrease in fO_2 of the experiments as the S^{2-} peaks become more dominant.

Figure 9 summarizes the S-XANES results for five of the glasses measured using the lowest radiation level (ΔFMQ+1.48, ΔFMQ+1.54, ΔFMQ+1.75, ΔFMQ+2.08, and ΔFMQ+3.3). The spectra shown are the result of 15–20 fly-scan spectra from different spots that have been merged. Similar to the intermediate and highest levels, the experiments conducted at ΔFMQ+1.75, ΔFMQ+2.08, and ΔFMQ+3.3 all show a dominant S^{6+} peak and minor to no S^{4+} peak. The intermediate fO_2 experiments at ΔFMQ+1.54 and ΔFMQ+1.48 have markedly lower intensity S^{6+} peaks and the appearance of intermediate to reduced S species at 2477.3 eV (S^{4+}) and ~2471 eV (S^{1-}), although they are more difficult to resolve given the lower signal/noise.

Estimated $S^{6+}/\Sigma S$ ratios

The ratio of oxidized S to total S ($S^{6+}/\Sigma S$) was calculated for spectra from all three radiation levels, reported in Tables 4, 5, and 6 and summarized in Figure 10. The highest radiation level $S^{6+}/\Sigma S$ ratios ranged from 0.72–0.74 at ΔFMQ+3.3, 0.75–0.84 at ΔFMQ+1.75, 0.25–0.27 at ΔFMQ+1, 0.20–0.46 at ΔFMQ+0.5, 0.17–0.22 at ΔFMQ+0, and 0.03–0.15 at ΔFMQ-0.7 (Table 4). The lowest level $S^{6+}/\Sigma S$ ratios were calculated to be 0.98 from the first 15 fly-scans at ΔFMQ+3.3, 0.98 from the first 3 fly-scans at ΔFMQ+2.08, 0.87 from the first 15 fly-scans at ΔFMQ+1.75, 0.52–0.54 from the first 20 fly-scans at ΔFMQ+1.54, and 0.38–0.52 from the first 20 fly-scans at ΔFMQ+1.48 (Table 5). The calculated $S^{6+}/\Sigma S$ ratios from the intermediate level varied from scan 1 to scan 2 and are plotted separately in Fig. 10. $S^{6+}/\Sigma S$ ranged from 0.82–0.92 and 0.73–0.76 for scans 1 and 2, respectively, at ΔFMQ+3.3, 0.74–0.77 for both scans 1 and 2 at ΔFMQ+1.75, from 0.13–0.16 and 0.16–0.21 for scans 1 and 2,

452 respectively, at ΔFMQ+1, 0.11–0.13 and 0.17–0.22 for scans 1 and 2, respectively, at
453 ΔFMQ+0.5, from 0.07–0.08 and 0.08–0.09 for scans 1 and 2, respectively, at ΔFMQ+0, and
454 0.07–0.08 and 0.13 for scans 1 and 2, respectively, at ΔFMQ-0.7 (Table 6).
455
456 **DISCUSSION**
457 **Quantifying beam damage**
458 Analyzing the same S-bearing dacitic glasses using three different radiation levels allows
459 us to compare the beam damage incurred at each level and estimate the exposure/time conditions
460 for S-XANES analyses. Starting with the highest level, spectra collected do not visibly change
461 much from scan 1 to 2 to 3, save for some growth in the S^{6+} peak in the more reduced spectra
462 (Fig. 3). This indicates that at or above photon flux densities of 1.0–4.5 x 10^{10} photons/sec per
463 μm^2, beam damage has reached a maximum after just a few minutes and does not continue to
464 alter the S speciation in the silicate glass to an observable degree. Given that a single ~12 minute
465 scan at the highest level is virtually indistinguishable from subsequent scans at that level and that
466 all but one time scan in Fig. 6 reach a constant intensity within one minute, we estimate that
467 within two minutes of analyses beam damage has occurred and significantly altered the S
468 oxidation states in the glass. Therefore, the threshold for beam damage at the highest radiation
469 level is estimated to be at least 1.2–5.4 x 10^{12} photons/μm^2. Importantly, any S-XANES
470 measurements on silicate glasses above this threshold will not show evidence for beam damage
471 even though it has occurred.
472 The intermediate radiation level considered in this study had a photon flux density that
473 ranged from 1.4–5.7 x 10^9 photons/sec per μm^2. In contrast to the highest level, spectra from
474 scans 1 and 2 collected at the intermediate level reveal significant changes in peak heights and

475 the appearance of peaks at intermediate S oxidation states over the time frame of ~9 minutes of
476 beam exposure. The consistent differences between the calculated $S^{6+}/\Sigma S$ ratios between scans 1
477 and 2 at the intermediate level are direct evidence of beam damage and allow us to semi-
478 quantitatively assess the amount of absorbed photons required to cause damage. To visualize the
479 difference in $S^{6+}/\Sigma S$ between scan 1 and 2 at the intermediate level, Figure 11 compares the
480 $S^{6+}/\Sigma S$ at each fO_2. Figure 11a shows that the $S^{6+}/\Sigma S$ of scan 1 is always lower than that of scan 2
481 for the more reduced experiments (ΔFMQ-0.7, ΔFMQ+0, ΔFMQ+0.5, ΔFMQ+1), while Figure
482 11b shows that the $S^{6+}/\Sigma S$ of scan 1 are higher than scan 2 for the more oxidized experiments
483 (ΔFMQ+2.08 and ΔFMQ+3.3). The intermediate fO_2 experiments (ΔFMQ+1.54, Fig. 11a;
484 ΔFMQ+1.75, Fig. 11b) do not show consistent increases or decreases from scan 1 to scan 2.
485 Figure 11 demonstrates that beam damage induces both oxidation and reduction of S over time in
486 the dacitic glass depending on the starting fO_2 of the experiment – for glasses that are relatively
487 reduced, beam exposure causes photo-oxidation; for glasses that are relatively oxidized, beam
488 exposure causes photo-reduction. However, at intermediate fO_2 (ΔFMQ+1.54 and ΔFMQ+1.75),
489 the direction of the change in $S^{6+}/\Sigma S$ is not consistent. For the most oxidized glasses the $S^{6+}/\Sigma S$
490 of scan 2 is an average of 13.5% lower than scan 1 at ΔFMQ+3.3 and an average of 8.9% lower
491 at ΔFMQ+2.08 (Table 6). For the more reduced glasses (at ΔFMQ-0.7, ΔFMQ+0, ΔFMQ+0.5,
492 and ΔFMQ+1) the average $S^{6+}/\Sigma S$ for scan 2 is 22–75% higher than scan 2 (Table 6). No
493 systematic increase or decrease in the percent difference between scans 1 and 2 exists for the
494 glasses analyzed in this study, pointing to a relatively unpredictable magnitude of change from
495 scan 1 to scan 2 of the intermediate level spectra. From Figures 2, 3, 10, and 11 it is evident that
496 the $S^{6+}/\Sigma S$ is significantly altered within 9 minutes of beam exposure using a photon flux density
497 of 1.41–5.69 x 10^9 photons/sec per μm^2.

However, understanding if scan 1 from the intermediate level represents the original, unaltered $S^{6+}/\Sigma S$ of the glass is a separate question. From the time scans shown in Figure 6 we observe the S^{6+} intensity decreasing while the S^{4+} and S^{2-} intensity increase over time on the most oxidized sample (ΔFMQ+3.3). This is evidence that the $S^{6+}/\Sigma S$ is altered during the first minutes of measurement at the intermediate level. We also observe a significant overlap in the total radiation received during scan 1 vs. scan 2 at the intermediate level: the average absorbed photons for scan 1 ranges from 7.63×10^{11} to 3.07×10^{12} photons/μm^2 after ~9 minutes and the average for scan 2 ranges from 1.53×10^{12} to 6.15×10^{12} photons/μm^2 after ~18 minutes (Supplementary Table S2). Therefore, we can estimate the beam damage threshold at the intermediate level to be 7.63×10^{11} to ~1.0×10^{12} photons/μm^2. This range is considered the least altered at the intermediate level since it represents the amount of absorbed photons that is between scan 1 and the lowest value of scan 2 at the intermediate level, as well as below the threshold estimated from the highest radiation level.

Finally, we consider the lowest radiation level: the spectra collected with a photon flux density of 2.0×10^7 photons/sec per μm^2. The nature of the fly-scan collection method made it easier to observe and quantify beam damage, although the lower flux density/higher S detection limit compared to the intermediate and highest levels made interpreting the lower-concentration intermediate to reduced spectra difficult. The $S^{6+}/\Sigma S$ calculated from oxidized (ΔFMQ+3.3, ΔFMQ+1.75) spectra collected using the lowest level are consistently higher than the $S^{6+}/\Sigma S$ calculated from the highest and intermediate levels (Fig. 10). The fact that we observe changes in the spectra from the averages of the first ≤ 15 scans compared to the last 3–20 scans (Figs. 2, 4, and 5) proves that beam damage alters the spectra collected at the lowest radiation level. Figure 4c compares the first 3 scans to the final 3 scans of 15 total and shows that after ~20 minutes of

beam exposure (12+ scans) the S^{6+} peak height has decreased relative to the first 3 scans. However, it is important to note that both spectra from Figure 4c yielded similar $S^{6+}/\Sigma S$ because neither the S^{4+} or S^{2-} peaks increased greatly within that time: 0.983 for the first 3 scans vs. 0.965 for the last 3 scans. We determine the absorbed photon threshold to be estimated at 1.44 x 10^{10} photons/μm^2 for the lowest radiation level, which corresponds to 12 fly-scans or ~20 minutes of beam interaction.

Similar to the intermediate radiation level, beam damage at the lowest level manifests as a decrease in the $S^{6+}/\Sigma S$ for intermediate to oxidized experiments (ΔFMQ+1.48, ΔFMQ+1.54, ΔFMQ+1.75, ΔFMQ+2.08, and ΔFMQ+3.3). Since the number of fly-scans can be grouped and merged over time to represent snapshots of the $S^{6+}/\Sigma S$ as a function of beam exposure, we plot the beam exposure time vs. the calculated $S^{6+}/\Sigma S$ for the glasses analyzed using fly-scans in Figure 12. While no systematic oxidation/reduction trend exists, evidenced by the differences in slopes between points, beam damage begins to affect the $S^{6+}/\Sigma S$ after < 25 minutes of beam exposure, consistent with observations described in the previous paragraph. The most oxidized experiment at ΔFMQ+3.3 showed the least change in the $S^{6+}/\Sigma S$ over time, while the experiment at ΔFMQ+1.75 showed the largest change over a shorter time frame (Fig. 12). Comparison of the fly-scans with a set of step scans collected at the lowest level showed a similar result: as one 48 minute step scan equals >27 fly-scans, the manifestation of beam damage already between scans 1 and 2 in Figure 5 is consistent with beam damage being observed after the absorption of > 1.44 x 10^{10} photons/μm^2.

Given all these observations, we conclude that the spectra that recorded the least amount of beam damage during this study were the first < 15 fly-scans from the lowest radiation level, as would be expected. At the photon flux density of 2.0 x 10^7 photons/second per μm^2, the photons

544 absorbed after 20 minutes (3–12 fly-scans) was between 6.3 x 10^9 to 1.44 x 10^{10} photons/μm^2
545 (Supplementary Table S2). This range represents the amount of absorbed radiation the dacitic
546 glass can take before the $S^{6+}/\Sigma S$ is altered significantly from its original value at the lowest
547 radiation level. However, the lower signal at lower flux limits measurements of lower
548 concentration samples such as the more reduced glasses in our experiments (< 0.025 wt% S).
549 Therefore, at a beamline with a photon flux density comparable to 2.0 x 10^7 photons/second per
550 μm^2, reduced samples (ΔFMQ < +1.5) cannot be measured reliably. Those measurements need to
551 be performed at a beamline with a higher photon flux density and consequently a higher S
552 fluorescence signal, as photon density limits permit. Another important result from this study is
553 that beam damage appears to level off after reaching a maximum. The S-XANES spectra from
554 scan 2 at the intermediate level and the scans from the highest level are overall similar (Figs. 2
555 and 3).
556
557 **Mechanisms of photo-oxidation and photo-reduction**
558 The existence of two types of radiation-induced changes, photo-oxidation of more
559 reduced glasses and photo-reduction of more oxidized glasses, complicates the conclusions
560 reached by previous authors investigating S-XANES beam damage on basaltic silicate glasses
561 (e.g., Wilke et al. 2008; Lerner et al., 2021). These mechanisms operate independently, or even
562 compete, and therefore likely differ in what photon flux density and time are necessary to impact
563 measured results in hydrous dacitic silicate glasses. The reduction of S^{6+} to S^{4+} shows the fastest
564 and largest magnitude change and is well documented in basaltic silicate glasses that are both
565 oxidized ($S^{6+}/\Sigma S = 1.0$) and reduced ($S^{6+}/\Sigma S = 0.04$–0.08; see Fig. 10 in Lerner et al., 2021). The
566 oxidation of S^{2-} to S^{6+} in more reduced silicate glasses ($\Delta FMQ \leq 1$) recognized in Figures 3 and

11, however, has not been documented for anhydrous or hydrous basaltic or andesitic silicate glasses. Understanding photo-oxidation processes are important because even a small amount of oxidation of S^{2-} to S^{6+} will impact the $S^{6+}/\Sigma S$ ratio owing to the small initial amount of S^{6+} in the more reduced samples. Wilke et al. (2008) report photo-oxidation of S^{2-} during S-XANES measurements taken on their hydrous soda-lime silicate glass (SiO_2 = 67.3 wt%, CaO = 7.7 wt%, Na_2O = 22.5 wt%, H_2O = 5 wt%, S = 2 wt%) equilibrated at ΔFMQ+0 conducted at the SLS LUCIA beamline. Because those authors did not observe photo-oxidation during analyses of their andesitic and basaltic silicate glasses at the ESRF, Wilke et al. (2008) attribute the oxidation to differences in beam intensity and/or the glass chemistry and stress that photon irradiation produces complex interactions and reorganizations in the local structural environment

Reaction of dissolved H_2O molecules in the silicate glass during Fe-XANES analysis has been shown to play a major role in the oxidation of Fe^{2+} to Fe^{3+} in basaltic silicate melts. Cottrell et al. (2018) detected photo-oxidation of Fe^{2+} and an increase in the $Fe^{2+}/\Sigma Fe$ in their hydrous basaltic silicate glasses and not in their anhydrous basaltic silicate glasses. Those authors' evidence points to the following photo-oxidation mechanism: 1) breaking of O–H bonds by incident ionizing radiation, 2) the loss of hydrogen, and 3) concomitant oxidation of Fe^{2+} to Fe^{3+}. Cottrell et al. (2018) tested the viability of that mechanism by subjecting one of their hydrous basaltic glasses (2.43 wt% H_2O) to a 2 x 2 μm beam of high photon flux (~1 x 10^{12} photons/sec) for 12 min. Subsequent mapping of the H_2O content of the area surrounding that spot via Fourier transform infrared spectroscopy show that the irradiated spot contained 900 ppm lower H_2O than a spot away from the damage zone (Fig. 10 in Cottrell et al., 2018). The test supports the photo-oxidation mechanism described above because it proved that water loss occurred during X-ray beam irradiation. While the energy range used for Fe-XANES is higher than that used for S-

XANES, it is important to note that beam size, total analysis time, and photon flux used in the test by Cottrell et al. (2018) are comparable to those used in this study, particularly to the high radiation level measurements.

Given that photo-oxidation involving the breaking of O–H bonds of dissolved H_2O has been shown to be the underlying mechanism responsible for the oxidation of Fe^{2+} to Fe^{3+} in hydrous basaltic silicate glasses, it is reasonable to assume that the same mechanism acts in hydrous dacitic glasses. We propose that the described photo-oxidation mechanism operates more efficiently in our hydrous dacitic silicate glass than in basaltic silicate glass for a number of reasons. First, even though Fe-XANES is conducted at three times higher energy than S-XANES, the absorbed radiation per unit volume is ~15.5 times smaller using lower energy X-rays (calculated absorption length of 4.8 μm at 2475 eV for S-XANES vs. 74.6 μm at 7100 eV for Fe-XANES using dacitic glass composition from the ΔFMQ+1 experiment). Second, the irradiation of lower energy X-rays tends to create more photo-electrons capable of damaging regions within and outside the illuminated beam volume than higher energy X-rays, which are more likely to be absorbed by heavier atoms that can fluoresce a portion of that energy out of the sample. Third, the absorption cross-section of H_2O (i.e., the probability of ionization by a photon) is 23.3 times larger at 2475 eV than at 7100 eV. Taken together, for the same flux density, radiation-induced changes are much more likely at the S *K*-edge than at the Fe *K*-edge. A reason photo-oxidation of S^{2-} has not been detected in basaltic silicate glasses could be due to the higher FeO^{tot} content, which may be preferentially oxidized and more easily detected because it requires only a single electron to oxidize Fe^{2+} instead of eight electrons to oxidize S^{2-}. The Fe-free soda-lime silicate glass of Wilke et al. (2008) that showed photo-oxidation of S^{2-} to S^{6+} is

612 further evidence that the Fe content of the silicate melt is the main parameter influencing the
613 detection of photo-oxidation of S^{2-} in silicate glasses.
614
615 **Comparing the measured sulfide-sulfate transition to thermodynamic predictions**
616 The transition from a sulfide- to sulfate-dominated silicate melt has been the focus of a
617 plethora of studies, and this study provides a unique opportunity to observe this change. As
618 discussed in Wallace and Carmichael (1994), Matthews et al. (1999), Metrich et al. (2009), Jugo
619 et al. (2010), Klimm et al. 2012, and Nash et al. (2019), the transition is defined by the following
620 redox reaction:
621 $$S^{2-} + 2O_2 = SO_4^{2-} \quad (1)$$
622 Oxygen plays the role of the electron acceptor during the oxidation of S^{2-} to S^{6+} and the
623 equilibrium constant expression of Eq. 1 is written as

$$K_1 = \frac{[a_{SO42-}]}{[a_{S2-}][fO_2]^2} \quad (2)$$

624
625
626 where K_1 is the equilibrium constant of Eq. 1 and a_i is the activity of component *i* in the silicate
627 melt. The form of Eq. 2 defines the functional shape of the sulfide-sulfate transition curve and
628 therefore the width of the transition in terms of fO_2. Assuming that the activities of S^{6+} and S^{2-}
629 can be described by their concentrations (*c*), the equilibrium constant expression can be
630 rearranged as:
631 $$\log(cSO_4^{2-}/cS^{2-}) = 2\log fO_2 + \log K_1 \quad (3)$$
632 From Eq. 3, the sulfide-sulfate transition is defined by a straight line, $y = 2x + b$, therefore the
633 ideal slope of the $S^{6+}/\Sigma S$ within the fO_2 range of the sulfide-sulfate transition is 2. It follows that
634 the $\log(S^{6+}/\Sigma S)$ calculated from the dacitic glasses of this study should have a slope of 2 when

This is the peer-reviewed, final accepted version for American Mineralogist, published by the Mineralogical Society of America.
The published version is subject to change. Cite as Authors (Year) Title. American Mineralogist, in press.
DOI: https://doi.org/10.2138/am-2022-8833. http://www.minsocam.org/

plotted against ΔFMQ (logfO_2 in Eq. 3) if the $S^{6+}/\Sigma S$ at run conditions was preserved during quench and has not been altered by beam damage. Figure 13a plots the log($S^{6+}/\Sigma S$) vs ΔFMQ for the three radiation levels and demonstrates that the log($S^{6+}/\Sigma S$) for scan 1 at the intermediate level falls closest to the ideal slope predicted by thermodynamics in Eq. 3 (m = 2, black solid line in Fig. 13a). Linear regressions applied to each set of points in the range of the sulfide-sulfate transition (ΔFMQ+1 to ΔFMQ+2; gray box in Fig. 13) in Table 7 show that scan 1 points from the intermediate level have a slope of 1.87, merged points from the highest level have a slope of 1.50, and the average of the first < 25 fly-scans at the lowest level have a slope of 2.49. In a comparable study on S speciation in experimentally produced basaltic melts at 1050°C and 200 MPa and a range of fO_2 (ΔFMQ-1.4 to ΔFMQ+2.7), Jugo et al. (2010) reports that log($S^{6+}/\Sigma S$) measured with S-XANES vs ΔFMQ for their samples produced a slope of 2.16. As argued in Jugo et al. (2010), we interpret the close agreement between the slope of log($S^{6+}/\Sigma S$) vs ΔFMQ of scan 1 from the intermediate level and the ideal slope predicted from thermodynamics to indicate that the S oxidation states in our dacitic melts at run conditions were preserved during rapid-quenching through the glass transition. Beam damage during S-XANES analyses only minimally affected the calculated $S^{6+}/\Sigma S$ of the glasses, even though the beam damage has likely altered the spectra slightly from scan 1 as discussed in section 4.1. The slope of the lowest level points is higher than that predicted by thermodynamics, but we suggest that the lack of data at lower fO_2 (ΔFMQ+1) is the main cause of this discrepancy since these spectra are the least altered from beam damage.

Since Fe is the only major element that is redox sensitive in silicate melts, oxidation-reduction reactions involving Fe and S are also important to consider. The relationship between S

and Fe oxidation states in silicate glasses can be described by the following electron-exchange reaction:

$$S^{2-} + 8Fe^{3+} = S^{6+} + 8Fe^{2+} \quad (4)$$

Equation 4 demonstrates that eight moles of Fe^{3+} are required to oxidize one mole of S^{2-} in the melt, or that one mole of S^{6+} can oxidize eight moles of Fe^{2+}, which implies a linear relationship between the logarithms of the activities of S^{6+}/S^{2-} and Fe^{3+}/Fe^{2+} with a gradient of 8 (e.g., Metrich et al., 2009; Nash et al. 2019). Figure 13b plots the $\log(S^{6+}/S^{2-})$ estimated using the Gaussian areas of the of S^{6+} and S^{2-} peaks obtained via S-XANES and the $\log(Fe^{3+}/Fe^{2+})$ calculated with the model of Kress and Carmichael (1991) using the spreadsheet of Iacovino (2021). The Kress and Carmichael (1991) model uses as input the T, P, fO_2, and major-element composition of the melt. The black solid line in Fig. 13b shows the ideal slope of 8 predicted by Eq. 4 and fits closely the points of scan 1 from the intermediate level within the sulfide-sulfate transition, as in Fig. 13a. We interpret the close fit to scan 1 from the intermediate level (m = 8.37) as further evidence that the S^{6+}/S^{2-} and Fe^{3+}/Fe^{2+} at run conditions were preserved during rapid-quench and that the $S^{6+}/\Sigma S$ measured during scan 1 at the intermediate level are not strongly affected by beam damage.

Solubility of S^{4+} in oxidized dacitic melts

Previous studies have focused almost entirely on mafic-intermediate silicate melt compositions and concluded that S^{4+} is not a stable species in those melt compositions (Wilke et al., 2008; Lerner et al., 2021). Our results indicate the presence of a S^{4+} peak in dacitic glasses at more oxidizing conditions (ΔFMQ > +1.75) at 300 MPa at all three radiation levels (Figs. 7–9). We note the S^{4+} spectral feature is present as a small peak in even the first scan conducted at the

lowest radiation level (Figs. 2, 9) in the more oxidized samples. In more reducing samples, however, the S^{4+} peak is overwhelmed by the broad S^{2-} peak when sulfide becomes the dominant oxidation state of S and is difficult to resolve absolutely. In Figure 6b, time scans performed at the energy of the S^{4+} peak show that the S^{4+} intensity decays over time for the highest radiation level while the S^{4+} intensity increases over time for the intermediate radiation level. This difference in S^{4+} intensity behavior could be pointing to differences in when or how quickly S^{4+} is produced during X-ray irradiation induced beam damage based on the photon flux density and exposure time.

We acknowledge that the acquisition of the XRF maps before S-XANES measurements and/or the pre-edge region of the spectra could have produced S^{4+} via the photo-reduction of S^{6+} by the time the X-ray reached the S^{4+} region of the spectra. However, the current measurement method of S-XANES cannot determine whether the S^{4+} peak feature was solely produced via instantaneous X-ray irradiation induced beam damage or if it is a true constituent dissolved in the dacitic glass that is highly sensitive to X-ray exposure. Since this discrepancy cannot be resolved using current S-XANES techniques, this study highlights the need for further investigation of beam damage systematics in silicate glasses using additional techniques.

IMPLICATIONS

Important differences in the solubility of different oxidation states of S are observed between dacitic silicate glasses and basaltic silicate glasses. The presence of an unmistakable S^{6+} peak (corresponding to 5–15% sulfate) in scan 1 spectra from the intermediate level at ΔFMQ-0.7, ΔFMQ+0, ΔFMQ+0.5, and ΔFMQ+1 distinguishes the S-XANES spectra in dacitic melts in this study from spectra collected on similarly reduced basaltic glasses. In Wilke et al. (2008),

703 Metrich et al. (2009), and Jugo et al. (2010), synthetic basaltic glass spectra only show peaks that
704 correspond to S^{2-} in their reduced experiments, with no S^{6+} peak. The natural basaltic glasses
705 analyzed by Jugo et al. (2010) at ΔFMQ-0.1 and ΔFMQ-1.4 also show no S^{6+} peak under
706 reducing conditions. Metrich et al. (2009) took this as evidence that minor surface oxidation
707 during sample preparation or measurement, as suggested by Fleet (2005), did not occur for their
708 samples. However, the presence of significant amounts of sulfate (8–9% S^{6+}) in some mid-ocean
709 ridge basaltic glasses around ΔFMQ+0 was confirmed after correcting for beam damage in
710 Lerner et al. (2021), supporting our finding that silicate glasses synthesized under reducing
711 conditions can contain non-trivial amounts of sulfate dissolved in the melt.
712 Comparing moderately oxidizing spectra from dacitic glasses and basaltic glasses, we
713 find that in our dacitic glasses S^{2-} is soluble at higher fO_2 compared to basaltic melts. In the Jugo
714 et al. (2010) study, there are no sulfide peaks in basaltic glasses at ΔFMQ+1.6, while in our
715 dacitic glasses ~40–60% of the S is present as sulfide at ΔFMQ+1.48 and ΔFMQ+1.54 in scan 1
716 from the intermediate level (Fig. 8) and the first 20 fly-scans from the lowest level (Fig. 9). The
717 implications for this difference include the increased solubility of elements that bond with sulfide
718 in the melt to higher fO_2 in dacitic melts (i.e., Au, Cu) and differences in the oxidation states of S
719 available to partition into an exsolved volatile phase (e.g., Zajacz et al., 2018; Jégo et al., 2016).
720 Therefore, dacitic melts can dissolve more sulfide at higher fO_2 and slightly more sulfate
721 at lower fO_2 than basaltic melts. The higher degree of melt polymerization and lower Fe content
722 in felsic silicate melts could play a role in the reactions governing the dissolution of S^{2-} and S^{6+},
723 as the lower proportion of non-bridging oxygens in felsic silicate melts may cause major element
724 cations with a 2+ charge (e.g., Ca, Mg, Mn) to bond with S^{2-} instead of with O^{2-}. Essentially, this
725 process could stabilize S^{2-} in felsic silicate melts to higher fO_2 compared to mafic silicate melts

726 which have a higher proportion of O^{2-} available for complexation. More work is required to fully
727 understand the complex interactions of elements in silicate melts as a function of melt
728 composition.

729 Figure 14 plots the regions of fO_2 estimated from mineral equilibria from a variety of
730 calc-alkaline, arc-related magmas (Lascar Volcano, Pinatubo, El Chichón, St. Helens) with the
731 least altered $S^{6+}/\Sigma S$ from scan 1 collected at the intermediate radiation level and the first ≤ 20
732 fly-scans collected at the lowest level. The blue and dark yellow lines are model non-linear least
733 squares fits of the intermediate and lowest level data, respectively. Table 8 contains the equations
734 and model estimates. Figure 14 shows that arc magmas can lie along the entire range of the
735 sulfide-sulfate transition. Matthews et al. (1994) note that Lascar Volcano, which spans a large
736 range of fO_2, had both Cu-Fe sulfide inclusions in ilmenite and anhydrite inclusions in magnetite.
737 The Pinatubo and El Chichón eruptive products both contain anhydrite, attesting to their oxidized
738 character (e.g., Bernard et al. 1991; Luhr 1990). This study demonstrates that the melt $S^{6+}/\Sigma S$ of
739 H_2O-saturated dacitic melts at 1000°C and 300 MPa can record the fO_2 of the system if the melt
740 was quenched rapidly through its glass transition temperature, and that observations from natural
741 arc magmas are broadly consistent with the variation in $S^{6+}/\Sigma S$ vs. fO_2. However, it is important
742 to note that more work is required to directly compare these experimental results with natural
743 silicate melts, as the effects of slow rate of cooling on the $S^{6+}/\Sigma S$ of the melt are not yet
744 understood.

745 Finally, the presented results underline the importance to carefully evaluate and address
746 the issues of radiation damage for each sample analyzed. Radiation damage can occur early even
747 at a very low radiation levels, rendering the onset of beam damage difficult to detect using higher
748 radiation levels. Unfortunately, minimizing the radiation dose is a trade-off with spectral quality.

One approach to overcome this would be to increase fluorescence photon detection through systems such as multielement detectors that cover a large solid angle. Another approach is to increase analysis speed, requiring faster detectors, in particular for glasses with low S concentrations and high levels of background scattering or fluorescence. In the interim, measurements of susceptible samples at conditions to minimize radiation damage require greater care and investment of time to obtain good results. Ultimately, much more work is needed to fully understand the onset and effects of beam damage caused by S-XANES analyses on silicate glasses and to understand and constrain the existence of the S^{4+} peak.

ACKNOWLEDGEMENTS

This research used resources of the Advanced Photon Source, a U.S. Department of Energy (DOE) Office of Science User Facility operated for the DOE Office of Science by Argonne National Laboratory under contract no. DE-AC02-06CH11357. We acknowledge the support of GeoSoilEnviroCARS (Sector 13), which is supported by the National Science Foundation–Earth Sciences (EAR-1128799), and the Department of Energy, Geosciences (DE-FG02-94ER14466). We acknowledge the Swiss Light Source at the Paul Scherrer Institut in Villigen, Switzerland, and the PHOENIX X07MB beamline for provision of synchrotron radiation beamtime. This research also used resources of the 8-BM TES beamline of the National Synchrotron Light Source II, a U.S. DOE Office of Science User Facility operated by Brookhaven National Laboratory under Contract No. DE-SC0012704, and support from the Tender Energy Microspectroscopy Consortium. We thank Owen K. Neill of the Electron Microanalysis Laboratory of the University of Michigan for assistance in obtaining high quality data from the EPMA. Financial support in the form of an International Institute Grant, a

Department of Earth and Environmental Sciences Turner Award, and Rackham Graduate Student Research Grant from the University of Michigan are gratefully acknowledged as well as a National Science Foundation Graduate Research Fellowship and Society of Economic Geologists Fellowship awarded to J.M.K. The experimental work was supported by DFG (German Science Foundation) project HO 1337/43 to F.H. A.C.S acknowledges support from NSF EAR 1924142 and 2214119. We thank editor Don Baker for his patience and help along with Kalotina Geraki and an anonymous reviewer for providing feedback and suggestions that greatly improved the work presented here.

REFERENCES CITED

Backnaes, L., Stelling, J., Behrens, H., Goettlicher, J., Mangold, S., Verheijen, O., Beerkens, R.G., and Deubener, J. (2008). Dissolution mechanisms of tetravalent sulphur in silicate melts: Evidences from sulphur *K*-edge XANES studies on glasses. Journal of the American Ceramics Society, 91, 721–727.

Bernard, A., Demaiffe, D., Mattielli, N., and Punongbayan, R.S. (1991). Anhydrite-bearing pumices from Mount Pinatubo: Further evidence for the existence of sulphur-rich silicic magmas. Nature, 354, 139–140.

Berndt, J., Liebske, C., Holtz, F., Freise, M., Nowak, M., Ziegenbein, D., Hurkuck, W., and Koepke, J. (2002). A combined rapid-quench and H_2-membrane setup for internally heated pressure vessels: Description and application for water solubility in basaltic melts. American Mineralogist, 87, 1717–1726.

Berry, A.J., O'Neill H.S.C., Scott D.R., Foran G.J., and Shelley J.M.G. (2006). The effect of composition on Cr^{2+}/Cr^{3+} in silicate melts. American Mineralogist, 91, 1901–1908.

795 Bonnin-Mosbah, M., Metrich, N., Susini, J., Salome, M., Massare, D., and Menez, B. (2002).
796 Micro X-ray absorption near edge structure at the sulfur and iron *K*-edges in natural
797 silicate glasses. Spectrochimica Acta Part B: Atomic Spectroscopy, 57(4), 711-725.
798 Cottrell, E., Lanzirotti, A., Mysen, B., Birner, S., Kelley, K., Botcharnikov, R.E., David, F., and
799 Newville, M. (2018). A Mössbauer-based XANES calibration for hydrous basalt glasses
800 reveals radiation-induced oxidation of Fe. American Mineralogist, 103, 489–501.
801 Evans, B., and Scaillet, B. (1997). The redox state of Pinatubo dacite and the ilmenite-hematite
802 solvus. American Mineralogist, 82(5-6), 625–629.
803 Fiege, A., Behrens, H., Holtz, F., and Adams, F. (2014). Kinetic vs. thermodynamic control of
804 degassing of H_2O–S ± Cl-bearing andesitic melts. Geochimica et Cosmochimica Acta,
805 125, 241–264.
806 Fleet, M.E. (2005). XANES spectroscopy of sulfur in earth materials. The Canadian
807 Mineralogist, 43, 1811–1838.
808 Fleet, M.E., Liu, X., Harmer, S.L., and King, P.L. (2005). Sulfur *K*-edge XANES spectroscopy:
809 Chemical state and content of sulfur in silicate glasses. The Canadian Mineralogist, 43,
810 1605–1618.
811 Iacovino, K. (2021). Ferric/Ferrous, Fe^{3+}/FeT, fO_2 Converter (Kress and Carmichael, 1991) (3.2).
812 Zenodo. https://doi.org/10.5281/zenodo.5907844, accessed February 23, 2022.
813 Jégo S., Nakamura, M., Kimura, J.-I., Iizuka, Y., Chang, Q., and Zellmer, G.F. (2016). Is gold
814 solubility subject to pressure variations in ascending arc magmas? Geochimica et
815 Cosmochimica Acta, 188, 224–243.

Jugo P.J., Wilke M., and Botcharnikov R.E. (2010). Sulfur K-edge XANES analysis of natural and synthetic basaltic glasses: Implications for S speciation and S content as function of oxygen fugacity. Geochimica et Cosmochimica Acta, 74, 5926–5938.

Klimm K., Kohn S., and Botcharnikov R.E. (2012a). The dissolution mechanism of sulphur in hydrous silicate melts I: Assessment of analytical techniques in determining the sulphur speciation in iron-free to iron-poor glasses. Chemical Geology, 322–323, 237–249.

Klimm K., Kohn S., and Botcharnikov R.E. (2012b). The dissolution mechanism of sulphur in hydrous silicate melts II: Solubility and speciation of sulphur in hydrous silicate melts as a function of fO_2. Chemical Geology, 322–323, 250–267.

Konecke, B.A., Fiege, A., Simon, A.C., Linsler, S., and Holtz, F. (2019). An experimental calibration of a sulfur-in-apatite oxybarometer for mafic systems. Geochimica et Cosmochimica Acta, 265, 242–258.

Konecke, B.A., Fiege, A., Simon, A.C., Parat, F., and Stechern, A. (2017). Co-variability of S^{6+}, S^{4+}, and S^{2-}in apatite as a function of oxidation state: Implications for a new oxybarometer. American Mineralogist, 102, 548–557.

Kress, V., and Carmichael, I. (1991). The compressibility of silicate liquids containing Fe_2O_3 and the effect of composition, temperature, oxygen fugacity, and pressure on their redox states. Contributions to Mineralogy and Petrology, 108, 82–92.

Lanzirotti, A., Sutton, S., Newville, M., and Head, E. (2022). Radiation-induced changes in vanadium speciation in basaltic glasses: Implications for oxybarometry measurements using vanadium *K*-edge X-ray absorption spectroscopy. American Mineralogist, 107, 729–738.

838 Li, D., Bancroft, G.M., Kasrai, M., Fleet, M.E., Feng, X., and Tan, K. (1995). S K- and L-edge
839 X-ray absorption spectroscopy of metal sulfides and sulfates: Applications in mineralogy
840 and geochemistry. The Canadian Mineralogist, 33, 949–960.
841 Luhr, J. (1990). Experimental phase relations of water- and sulfur-saturated arc magmas and the
842 1982 eruptions of El Chichón Volcano. Journal of Petrology, 31(5), 1071–1114.
843 Matthews, S.J., Jones, A.P., and Beard, A.D. (1994). Buffering of melt oxygen fugacity by
844 sulphur redox reactions in calc-alkaline magmas. Journal of the Geological Society of
845 London, 151, 815–823.
846 Metrich, N., Berry, A., O'Neill, H.S.C., and Susini, J. (2009). The oxidation state of sulfur in
847 synthetic and natural glasses determined by X-ray absorption spectroscopy. Geochimica
848 et Cosmochimica Acta, 73, 2382–2399.
849 Metrich, N., Bonnin-Mosbah, M., Susini, J., Menez, B., and Galoisy, L. (2002). Presence of
850 sulfite (S^{IV}) in arc magmas: Implications for volcanic sulfur emissions. Geophysical
851 Research Letters, 29(11), 4.
852 Michaud, J.A-S., Pichavant, M., and Villaros, A. (2021). Rare elements enrichment in crustal
853 peraluminous magmas: insights from partial melting experiments. Contributions to
854 Mineralogy and Petrology, 176, 96.
855 Nash, W.M., Smythe, D.J., and Wood, B.J. (2019). Compositional and temperature effects on
856 sulfur speciation and solubility in silicate melts. Earth and Planetary Science Letters, 507,
857 187–198.
858 Newman, S., and Lowenstern, J.B. (2002). VolatileCalc: A silicate melt–H_2O–CO_2 solution
859 model written in Visual Basic for Excel. Computational Geosciences, 28, 597–604.

Northrup, P. (2019). The TES beamline (8-BM) at the NSLS-II: Tender-energy spatially resolved X-ray absorption spectroscopy and X-ray fluorescence imaging. Journal of Synchrotron Radiation, 26, 11.

Paris, E., Giuli, G., Carroll, M., and Davoli, I. (2001). The valence and speciation of sulfur in glasses by X-ray absorption spectroscopy. The Canadian Mineralogist, 39(2), 331–339.

Ravel, B., and Newville, M. (2005). ATHENA, ARTEMIS, HEPHAESTUS: Data analysis for X-ray absorption spectroscopy using IFEFFIT. Journal of Synchrotron Radiation, 12, 537-541.

Ruprecht, P., Bergantz, G.W., Cooper, K.M., and Hildreth, W. (2012). The crustal magma storage system of Volcán Quizapu, Chile, and the effects of magma mixing on magma diversity. Journal of Petrology, 53, 801–840.

Scaillet, B., Pichavant, M., Roux, J., Humbert, G., and Lefevre, A. (1992). Improvements of the Shaw membrane technique for measurement and control of fH_2 at high temperatures and pressures. American Mineralogist, 77, 647–655.

Sutton, S.R., Lanzirotti, A., Newville, M., Rivers, M.L., Eng, P., and Lefticariu, L. (2017). Spatially Resolved Elemental Analysis, Spectroscopy and Diffraction at the GSECARS Sector at the Advanced Photon Source. Journal of Environmental Quality, 46, 1158–1165.

Wallace P.J., and Carmichael I.S.E. (1994). S speciation in submarine basaltic glasses as determined by measurements of S $K\alpha$ X-ray wavelength shifts. American Mineralogist, 79, 161–167.

Wilke, M., Jugo, P.J., Klimm, K., Susini, J., Botcharnikov, R., Kohn, S.C. and Janousch, M. (2008). The origin of S^{4+} detected in silicate glasses by XANES. American Mineralogist, 93, 235–240.

883 Wojdyr, M. (2010). Fityk: a general-purpose peak fitting program. Journal of Applied
884 Crystallography, 43, 1126–1128.
885 Zajacz, Z., Candela, P.A., Piccoli, P.M., and Sanchez-Valle, C. (2012). The partitioning of sulfur
886 and chlorine between andesite melts and magmatic volatiles and the exchange
887 coefficients of major cations. Geochimica et Cosmochimica Acta, 89, 81–101.
888 Zajacz, Z., Candela, P.A., Piccoli, P.M., Sanchez-Valle, C., and Walle, M. (2013). Solubility and
889 partitioning behavior of Au, Cu, Ag and reduced S in magmas. Geochimica et
890 Cosmochimica Acta, 112, 288–304.

TABLES

Table 1. Experimental conditions

$logfO_2$[a]	Sample ID	Initial bulk S content	pH_2 initial[b]	SCSS/SCAS reached?[c]	Phase assemblage[d]
ΔFMQ-0.7	QD7-3	0.28 wt%	11.9	SCSS	gl - ap - fl - spl - FeS
ΔFMQ+0	QD4-6	0.28 wt%	5.39	SCSS	gl - ap - fl - spl - FeS
ΔFMQ+0.5	QD3-5	0.28 wt%	3.03	SCSS	gl - ap - fl - spl - FeS
ΔFMQ+1	QD1-4	0.28 wt%	1.82	SCSS	gl - ap - fl - spl - FeS
ΔFMQ+1.48	QD8-4	0.38 wt%	1.03	SCSS	gl - ap - fl - spl - FeS
ΔFMQ+1.54	QD10-1	0.38 wt%	0.71	SCSS	gl - ap - fl - spl - FeS
ΔFMQ+1.75	QD6-4	0.28 wt%	0.81	no	gl - ap - fl - spl
ΔFMQ+2.08	QD9-3	0.28 wt%	0.53	no	gl - ap - fl - spl
ΔFMQ+2.08	QD9-4	0.38 wt%	0.53	no	gl - ap - fl - spl
ΔFMQ+3.3	QD2-5	0.28 wt%	0	SCAS	gl - ap - fl - mag - anh
ΔFMQ+3.3	QD-305*	0.57 wt%	0	SCAS	gl - ap - fl - mag - anh

[a] log fO_2 reported relative to the FMQ mineral redox buffer.

[b] Partial pressure of hydrogen (pH_2) in bars added to the vessel before bringing the experiments up to run temperature and pressure. Calculated assuming a water activity of one inside the capsule as all experiments were H_2O-saturated.

[c] Fe-sulfide indicates melt reached SCSS (S content at sulfide-saturation); anhydrite indicates melt reached SCAS (S content at anhydrite-saturation). 'No' indicates melt was both sulfide- and sulfate-undersaturated.

[d] gl – silicate glass; ap – apatite; fl – fluid phase; FeS – Fe-sulfide melt; spl – spinel; mag – magnetite; anh – anhydrite.

* Redox equilibrium test described in text.

This is the peer-reviewed, final accepted version for American Mineralogist, published by the Mineralogical Society of America.
The published version is subject to change. Cite as Authors (Year) Title. American Mineralogist, in press.
DOI: https://doi.org/10.2138/am-2022-8833. http://www.minsocam.org/

895 **Table 2.** Composition of dacitic glasses

Sample	QD7-3	QD4-6	QD3-5	QD1-4	QD8-4	QD10-1	QD6-4	QD9-3	QD9-4	QD2-5
n[a]	39	14	15	18	13	11	28	14	15	24
SiO_2	62.2±0.10	63.04±0.13	63.04±0.10	62.82±0.21	62.95±0.07	62.78±0.11	62.13±0.11	63.27±0.12	62.47±0.13	63.26±0.17
Al_2O_3	15.79±0.04	15.93±0.07	16.00±0.04	15.74±0.06	15.32±0.04	15.46±0.07	15.60±0.03	15.64±0.06	15.33±0.06	15.64±0.05
TiO_2	0.50±0.01	0.51±0.01	0.50±0.01	0.49±0.01	0.50±0.01	0.51±0.02	0.50±0.01	0.49±0.01	0.50±0.01	0.48±0.01
FeO^{tot}	2.35±0.01	2.68±0.02	2.79±0.02	3.03±0.02	3.54±0.02	3.50±0.03	3.33±0.02	3.39±0.02	3.52±0.02	3.31±0.01
MgO	0.79±0.01	0.81±0.01	0.81±0.00	0.80±0.01	0.80±0.01	0.80±0.00	0.80±0.01	0.78±0.01	0.79±0.01	0.77±0.00
CaO	2.61±0.01	2.65±0.02	2.62±0.02	2.65±0.02	2.74±0.02	2.73±0.03	2.73±0.02	2.76±0.03	2.84±0.02	2.71±0.01
Na_2O	4.56±0.03	4.69±0.04	4.67±0.04	4.57±0.04	4.36±0.09	4.38±0.11	4.52±0.02	4.46±0.04	4.38±0.03	4.55±0.03
K_2O	3.26±0.01	3.22±0.02	3.27±0.02	3.26±0.02	3.20±0.02	3.20±0.02	3.26±0.01	3.23±0.02	3.17±0.01	3.22±0.02
P_2O_5	0.38±0.01	0.36±0.01	0.37±0.01	0.40±0.01	0.52±0.01	0.46±0.02	0.48±0.01	0.48±0.02	0.52±0.01	0.58±0.01
MnO	0.08±0.01	0.08±0.01	0.08±0.01	0.08±0.00	0.07±0.01	0.07±0.01	0.08±0.00	0.07±0.01	0.09±0.01	0.08±0.00
S	0.02303±0.0005	0.02083±0.0003	0.0191±0.0003	0.0244±0.0005	0.0196±0.0025	0.0505±0.0037	0.0551±0.0024	0.0307±0.0024	0.1045±0.0059	0.1138±0.0005
Cl	0.068±0.001	0.070±0.001	0.068±0.001	0.068±0.001	0.071±0.001	0.071±0.001	0.068±0.001	0.069±0.001	0.070±0.001	0.067±0.001
Total[b]	92.63±0.12	94.073±0.19	94.273±0.15	93.953±0.28	94.093±0.12	94.083±0.15	93.563±0.13	94.713±0.15	93.893±0.17	94.893±0.23
H_2O[c]	7.37	5.93	5.73	6.05	5.91	5.92	6.44	5.29	6.11	5.11

[a] Number of EPMA analyses.

[b] Totals calculated as the sum of all major and minor oxides and elements.

[c] H_2O content estimated by difference.

896

897

This is the peer-reviewed, final accepted version for American Mineralogist, published by the Mineralogical Society of America.
The published version is subject to change. Cite as Authors (Year) Title. American Mineralogist, in press.
DOI: https://doi.org/10.2138/am-2022-8833. http://www.minsocam.org/

898 **Table 3.** Beamline and S-XANES measurement details

		Advanced Photon Source (APS)	Swiss Light Source (SLS)	National Synchrotron Light Source II (NSLS-II)
Beamline		GSECARS 13-ID-E	PHOENIX X07MA/B	8-BM TES
Energy range		2.3–28 keV	0.35–8.0 keV	2.0–5.5 keV
X-ray source		undulator	undulator	bend magnet
Beam size		2 x 2 µm	3–4 µm diameter	4 x 8 to 7 x 14 µm
Calibration energy[a]		2481.8 eV	2482 eV	2481 eV
XRF maps	Detector dwell time & pixel size	0.02 sec per 2 x 2 µm pixel	1 sec per 3 x 3 µm pixel	0.1–0.3 sec per 2.8–12 µm pixel
	Energy[b]	2482 eV	2482 eV	2700 eV
Single scan duration		~9 min	~12 min	~1.75 min fly-scan / ~48 min step scan
Radiation level		intermediate	high	low
Photon flux density (photons/sec/µm^2)[c]		1.4–5.7 x 10^9	1.0–4.5 x 10^{10}	2.0 x 10^7
Sample environment		He gas (1 atm)	vacuum	He gas (1 atm)
Dwell time & step size	Pre-edge	3 sec per 1 eV step	1 sec per 2 eV step	1.2 sec per 1 eV
	Edge	3 sec per 0.3 eV step	2 sec per 0.3 eV step	0.3 sec per 0.25 eV
	Post-edge	3 sec per 2 eV step	1 sec per 2 eV step	1.2 sec per 1.0 eV

[a] The energy at the beamlines was calibrated to the ~2482 eV white line of sulfate using clear double-sided sticky tape at the APS, powdered $CaSO_4$ at the SLS, and Durango apatite at the NSLS-II.

[b] Energy at which the X-ray fluorescence (XRF) maps were collected.

[c] See section 2.3 and Supplementary Table S2 for more information.

899

900

This is the peer-reviewed, final accepted version for American Mineralogist, published by the Mineralogical Society of America.
The published version is subject to change. Cite as Authors (Year) Title. American Mineralogist, in press.
DOI: https://doi.org/10.2138/am-2022-8833. http://www.minsocam.org/

901 **Table 4.** $S^{6+}/\Sigma S$ from the highest photon flux density

Point*	fO_2	$S^{6+}/\Sigma S$
QD2-5r_1_01	ΔFMQ+3.3	0.74
QD2-5r_1_02	ΔFMQ+3.3	0.73
QD2-5r_1_03	ΔFMQ+3.3	0.72
QD2-5r_2_01	ΔFMQ+3.3	0.74
QD2-5r_2_02	ΔFMQ+3.3	0.74
QD2-5r_2_03	ΔFMQ+3.3	0.72
QD6-4_1_01	ΔFMQ+1.75	0.79
QD6-4_1_02	ΔFMQ+1.75	0.81
QD6-4_1_03	ΔFMQ+1.75	0.81
QD6-4_2_01	ΔFMQ+1.75	0.82
QD6-4_2_03	ΔFMQ+1.75	0.76
QD6-4_2_04	ΔFMQ+1.75	0.84
QD6-4_2_05	ΔFMQ+1.75	0.75
QD1-4_1_01	ΔFMQ+1	0.26
QD1-4_1_03	ΔFMQ+1	0.27
QD1-4_1_04	ΔFMQ+1	0.26
QD1-4_1_05	ΔFMQ+1	0.26
QD1-4_1_06	ΔFMQ+1	0.25
QD3-5_1_01	ΔFMQ+0.5	0.20
QD3-5_1_02	ΔFMQ+0.5	0.22
QD3-5_1_04	ΔFMQ+0.5	0.22
QD3-5_2_06	ΔFMQ+0.5	0.46
QD3-5_2_08	ΔFMQ+0.5	0.29
QD4-6_1_01	ΔFMQ+0	0.22
QD4-6_1_02	ΔFMQ+0	0.20
QD4-6_1_03	ΔFMQ+0	0.19
QD4-6_1_04	ΔFMQ+0	0.17
QD4-6_1_05	ΔFMQ+0	0.18
QD4-6_1_07	ΔFMQ+0	0.20
QD7-3_1_01	ΔFMQ-0.7	0.12
QD7-3_1_02	ΔFMQ-0.7	0.13
QD7-3_1_03	ΔFMQ-0.7	0.15
QD7-3_2_04	ΔFMQ-0.7	0.13
QD7-3_2_05	ΔFMQ-0.7	0.10
QD7-3_2_06	ΔFMQ-0.7	0.04
QD7-3_2_07	ΔFMQ-0.7	0.03

* All points were analyzed using 3 step scans except for the QD4-6 and QD7-3 series, which used 2 for each point. Each scan was ~12 min.

902

903

This is the peer-reviewed, final accepted version for American Mineralogist, published by the Mineralogical Society of America.
The published version is subject to change. Cite as Authors (Year) Title. American Mineralogist, in press.
DOI: https://doi.org/10.2138/am-2022-8833. http://www.minsocam.org/

904 **Table 5.** $S^{6+}/\Sigma S$ from the lowest photon flux density

Point	fO_2	Beam size (µm)	Total scans[a]	first scans[b]			last scans[b]			Differ-ence	Percent differ-ence
				n	t (min)	$S^{6+}/\Sigma S$	n	t (min)	$S^{6+}/\Sigma S$		
QD2-5	ΔFMQ+3.3	4 x 8	100	50	75	0.96	50	150	0.94	0.03	2.63
QD9-4_1	ΔFMQ+2.08	5 x 10	15	3	4.5	0.98	–	–	–	–	–
QD9-4_2step	ΔFMQ+2.08	5 x 10	14	1	48	0.98	1	672	0.82	0.16	16.34
QD6-4_12	ΔFMQ+1.75	4 x 8	63	15	26.3	0.87	15	110	0.87	0.00	0.41
QD10-1_1	ΔFMQ+1.54	5 x 10	94	20	30	0.52	20	141	0.48	0.04	8.21
QD10-1_2	ΔFMQ+1.54	5 x 10	41	20	30	0.54	20	61.5	0.53	0.01	1.73
QD8-4_1	ΔFMQ+1.48	5 x 10	44	20	30	0.52	20	66	0.46	0.06	11.37
QD8-4_2	ΔFMQ+1.48	7 x 14	25	20	30	0.38	–	–	–	–	–

[a] Total number of scans taken. All points were analyzed by fly-scans (~1.75 min/scan) except for QD9-4_2step, which was analyzed using step scans that were ~48 min/scan.

[b] Scans are divided into 'first scans', where the $S^{6+}/\Sigma S$ was calculated from the first *n* merged spectra, and 'last scans', which were calculated from the final *n* merged spectra. Points with total scans ≤ 30 were not split into first and last scans as beam damage is observed after > 30 fly-scans.

905

906

This is the peer-reviewed, final accepted version for American Mineralogist, published by the Mineralogical Society of America.
The published version is subject to change. Cite as Authors (Year) Title. American Mineralogist, in press.
DOI: https://doi.org/10.2138/am-2022-8833. http://www.minsocam.org/

907 **Table 6.** $S^{6+}/\Sigma S$ from the intermediate photon flux density

Point[a]	fO_2	$S^{6+}/\Sigma S$		Difference	Percent difference[b]
		Scan 1	Scan 2		
QD2-5_1_gl05	ΔFMQ+3.3	0.92	0.76	0.16	17.12
QD2-5_3_gl01	ΔFMQ+3.3	0.83	0.73	0.10	11.74
QD2-5_3_gl02	ΔFMQ+3.3	0.88	0.74	0.13	15.18
QD2-5_3_gl06	ΔFMQ+3.3	0.87	0.76	0.11	12.85
QD2-5_3_gl07	ΔFMQ+3.3	0.83	0.74	0.09	10.49
QD9-3_gl01	ΔFMQ+2.08	0.88	0.78	0.10	11.26
QD9-3_gl02	ΔFMQ+2.08	0.85	0.78	0.08	8.95
QD9-3_gl03	ΔFMQ+2.08	0.82	0.77	0.05	6.08
QD9-3_gl04	ΔFMQ+2.08	0.90	0.81	0.09	9.99
QD9-3_gl05	ΔFMQ+2.08	0.81	0.74	0.07	8.63
QD6-4_gl01	ΔFMQ+1.75	0.77	0.74	0.03	3.41
QD6-4_gl06	ΔFMQ+1.75	0.74	0.74	0.00	-0.16
QD10-1_gl01	ΔFMQ+1.54	0.61	0.55	0.06	9.41
QD10-1_gl02	ΔFMQ+1.54	0.36	0.40	-0.04	-11.48
QD10-1_gl03	ΔFMQ+1.54	0.42	0.47	-0.05	-11.88
QD10-1_gl04	ΔFMQ+1.54	0.38	0.34	0.03	8.74
QD10-1_gl05	ΔFMQ+1.54	0.37	0.36	0.01	2.57
QD8-4_gl01	ΔFMQ+1.48	0.44	–	–	–
QD8-4_gl02	ΔFMQ+1.48	0.40	–	–	–
QD8-4_gl03	ΔFMQ+1.48	0.48	–	–	–
QD8-4_gl04	ΔFMQ+1.48	0.41	–	–	–
QD8-4_gl05	ΔFMQ+1.48	0.48	–	–	–
QD1-4_gl01	ΔFMQ+1	0.17	0.21	-0.04	-26.58
QD1-4_gl05	ΔFMQ+1	0.13	0.16	-0.03	-23.80
QD3-5_gl01	ΔFMQ+0.5	0.12	0.22	-0.10	-79.45
QD3-5_gl06	ΔFMQ+0.5	0.12	0.17	-0.05	-44.24
QD3-5_gl07	ΔFMQ+0.5	0.13	0.20	-0.07	-57.12
QD4-6_gl01	ΔFMQ+0	0.07	0.09	-0.02	-20.62
QD4-6_gl06	ΔFMQ+0	0.07	0.09	-0.02	-24.53
QD7-3_gl01	ΔFMQ-0.7	0.07	0.13	-0.06	-88.70
QD7-3_gl06	ΔFMQ-0.7	0.08	0.13	-0.05	-62.94

[a] Two scans were collected at each point except for the QD8-4 series, where only one scan was taken per point. Each scan was ~9 min.
[b] Where positive, scan 1 had a higher $S^{6+}/\Sigma S$ than scan 2; where negative, scan 1 had a lower $S^{6+}/\Sigma S$ than scan 2.

908

909

This is the peer-reviewed, final accepted version for American Mineralogist, published by the Mineralogical Society of America.
The published version is subject to change. Cite as Authors (Year) Title. American Mineralogist, in press.
DOI: https://doi.org/10.2138/am-2022-8833. http://www.minsocam.org/

910 **Table 7.** Linear regressions of data to assess fit to thermodynamic predictions

Relationship	Radiation level	n[a]	Slope				Intercept				Adjusted R^2 [d]	Residual SE[e]
			m	SE	t value[b]	Pr(>|t|)[c]	b	SE	t value[b]	Pr(>|t|)[c]		
$\log(S^{6+}/\Sigma S)$ vs. ΔFMQ (Fig. 12a)	int.	#	1.87	0.21	8.74	1.50E-06	-3.64	0.32	-11.46	8.04E-08	0.853	0.169
	high	#	1.50	0.03	50.73	2.14E-13	-2.85	0.04	-64.97	1.82E-14	0.996	0.038
	low	6	3.80	0.40	9.42	2.54E-03	-6.56	0.59	-11.07	1.58E-03	0.956	0.222
$\log(S^{6+}/S^{2-})$ vs. $\log(Fe^{3+}/Fe^{2+})$ (Fig. 12b)	int.	#	8.37	1.05	8.01	3.72E-06	7.21	0.93	7.71	5.46E-06	0.829	0.365
	high	#	3.33	0.07	50.73	2.14E-13	2.28	0.06	38.22	3.59E-12	0.996	0.038
	low	6	14.08	1.45	9.73	2.31E-03	12.44	1.31	9.51	2.46E-03	0.959	0.353

[a] number of data points included in regression.

[b] Estimate divided by standard error (SE).

[c] Probability of exceeding that observed.

[d] R^2 value adjusted for the number of predictors.

[e] Standard deviation of the residuals.

911

912

913

914 **Table 8.** Model estimates for the sigmoid function fits of $S^{6+}/\Sigma S$ vs. ΔFMQ

915

Int. level scan 1 fit (blue line in Fig. 13)				
Equation	$\frac{S^{6+}}{\Sigma S} = \frac{c}{(1 + \exp(-a*fO_2 + b)) + d}$			
	$d = 0.085$[a]			
	Estimate	**SE**	**t value**	**Pr(>|t|)**
a	6.46	1.35	4.80	3.01E-03
b	9.91	2.04	4.85	2.86E-03
c	0.79	0.03	24.92	2.75E-07
Lowest level first ≤ 20 scans fit (dark yellow line in Fig. 13)				
Equation	$\frac{S^{6+}}{\Sigma S} = \frac{c}{(1 + \exp(-a*fO_2 + b)) + d}$			
	$d = 0.085$[a]			
	Estimate	**SE**	**t value**	**Pr(>|t|)**
a	7.31	2.15	3.40	7.68E-02
b	11.10	3.26	3.41	7.64E-02
c	0.91	0.04	21.21	2.21E-03

[a] The lower bound was fixed at the same value for both sigmoid functions.

916

917

FIGURE CAPTIONS

Figure 1. Backscattered electron (BSE) image of a representative run product, QD9-4 equilibrated at ΔFMQ+2.08. All run products contained glass (gl), apatite (ap), a micrometer-sized spinel mineral (not pictured), and an exsolved volatile phase (bub) at run conditions. Fe-sulfide and anhydrite were present in reducing (ΔFMQ < 1.6) and oxidizing (ΔFMQ+3.3) conditions, respectively.

Figure 2. Comparison of normalized spectra from all three radiation levels for samples at ΔFMQ+3.3 (**a**) and ΔFMQ+1.75 (**b**). Spectra are color-coded for each radiation level, with the darkest color for each being the first scan and lighter colors being subsequent scans. The lowest level spectra were acquired using fly-scans (~1.75 min/scan); the intermediate and highest levels using step scans (~9 and ~12 min/scan, respectively). The peak positions for S^{6+} (2482 eV), S^{4+} (2477.6 eV), and S^{2-} (2476.5 eV and 2470.3 eV) are shown as the solid, dashed, and dotted vertical lines, respectively, and labeled in (**b**).

Figure 3. Normalized spectra of S-XANES step scan measurements on dacitic glass from the highest radiation level (**a, c, e, g**; ~12 min/scan) and the intermediate radiation level (**b, d, f, h**; ~9 min/scan) for the more reducing experiments (ΔFMQ-0.7 to ΔFMQ+1). Two or three scans were taken per point to monitor for changes in peak intensity over time. Colors are the same as in Fig. 1, with the darkest color being scan 1 and the lighter colors being subsequent scans. Vertical lines are the same as in Fig. 1. Spectra from the highest level show minor changes in peak intensities from scan to scan, while spectra from the intermediate level show greater peak intensity differences between the first and second scan. Arrows illustrate the direction of change for certain peaks from scan 1 to later scans.

Figure 4. Normalized spectra collected on experiments conducted at ΔFMQ+1.48 (**a**), ΔFMQ+1.54 (**b**), and ΔFMQ+2.08 (QD9-4; **c**) dacitic glasses at the lowest radiation level using fly-scans of ~1.75 minutes/scan. Dark yellow line is the average of the first 20 (**a-b**) or 3 (**c**) scans collected at a single point while the light yellow line is the average of the last 20 (**a-b**) or 3 (**c**) scans collected at that same point. Vertical lines and arrows are the same as in Figs. 1 and 2; *n* shows the total number of scans collected for each spot.

Figure 5. Normalized spectra collected using step scans (~48 minutes/scan) at the lowest radiation level at ΔFMQ+2.08 (QD9-4, the same sample as Fig. 4c). Darkest yellow line is step scan 1, medium yellow line is step scan 2, and lightest yellow line is step scan #14. Lines and arrows are as described in Figs. 1 and 2.

Figure 6. Time scans on experiments conducted at ΔFMQ+3.3 comparing the S intensity changes over time for S^{6+} (**a**), S^{4+} (**b**), and S^{2-} (**c**) between the highest (red) and intermediate (blue) levels. Energy for (**a**) was 2482 eV, energy for (**b**) was 2477 eV, and energy for (**c**) was 2470 eV. The vertical axis shows the relative change in the intensity for each S oxidation state over time; the intensity of the first analysis point plots at a value of 1.0. The values above or below each line in 6b show the range of the total photons absorbed over the 5 minute duration of the scan, with colors corresponding to the radiation level. The values are the same in 6a and c.

Figure 7. Normalized and merged spectra from five samples (ΔFMQ-0.7, ΔFMQ+0, ΔFMQ+0.5, ΔFMQ+1, ΔFMQ+1.75, and ΔFMQ+3.3) measured at the highest radiation level. The number of

spectra merged for each fO_2 is indicated by *n* on the left side of the figure; acquisition time for each spectra is ~12 min. Vertical lines show peak positions as described in Fig. 1.

Figure 8. Normalized and merged spectra from nine samples (ΔFMQ-0.7, ΔFMQ+0, ΔFMQ+0.5, ΔFMQ+1, ΔFMQ+1.48, ΔFMQ+1.54, ΔFMQ+1.75, ΔFMQ+2.08, and ΔFMQ+3.3) measured at the intermediate radiation level. Note that only spectra from scan 1 are plotted here; *n* indicates the number of ~9 min scans merged for each fO_2. Vertical lines show peak positions as described in Fig. 1.

Figure 9. Normalized and merged spectra from five samples (ΔFMQ+1.48, ΔFMQ+1.54, ΔFMQ+1.75, ΔFMQ+2.08, and ΔFMQ+3.3) measured at the lowest radiation level. Note that only results from the fly-scans (~1.75 min/scan) are shown here, with *n* indicating the number of fly-scans merged for each fO_2. Vertical lines show peak positions as described in Fig. 1.

Figure 10. $S^{6+}/\sum S$ ratios for all beamlines against ΔFMQ. The data for the highest level consist of all merged spectra collected at the same point and same ΔFMQ. Spectra collected at the intermediate level are split into the average $S^{6+}/\sum S$ for scan 1 (dark blue, up-pointing triangles) and scan 2 (light blue, down-pointing triangles). The lowest level estimates include only results from the first ≤ 20 fly-scans. Standard error bars are smaller than the symbol size except where visible and were calculated using multiple $S^{6+}/\sum S$ determined by fitting spectra from different spot analyses at each fO_2 and radiation level (see Tables 4, 5, and 6).

Figure 11. Plots showing the effect of beam damage on the $S^{6+}/\sum S$ ratios vs. ΔFMQ collected at the intermediate level. In (**a**), five of the most reducing samples are shown (ΔFMQ+1.54, ΔFMQ+1, ΔFMQ+0.5, ΔFMQ+0, ΔFMQ-0.7); in (**b**), the three most oxidizing samples (ΔFMQ+1.75, ΔFMQ+2.08, ΔFMQ+3.3). As the ΔFMQ+1.48 experiment had only one scan taken at each point, it is not plotted here. Note that in (**a**) beam damage generally manifests as an increase in the $S^{6+}/\sum S$ ratio while in (**b**) it manifests as a decrease. In both panels curved lines connect scans made on the same point. Points are spread out at a single fO_2 to improve readability; red numbers above points depict the average photon density for scan 1 in photons/μm^2.

Figure 12. Minutes of beam exposure vs. the $S^{6+}/\Sigma S$ ratio for fly-scans collected at the lowest radiation level. The points represent a number of fly-scans converted to time in minutes to quantify the beam damage incurred at each fO_2. Lines connect measurements from the same point at the same fO_2, with the first point(s) being the average $S^{6+}/\Sigma S$ of all scans from time = 0 to the time of the point; the second and third points show the average of scans from the time of the subsequent connected point to the next point. The photon flux density for all points was ~2.0 x 10^7 photons/sec per μm^2 and the beam size was 4 x 8 μm for all points except for those at ΔFMQ+1.48, ΔFMQ+1.54, and ΔFMQ+2.08, which had a beam size of 5 x 10 μm.

Figure 13. Comparison of data to the thermodynamic predictions within the sulfide-sulfate transition. In (**a**), the $\log(S^{6+}/\Sigma S)$ vs ΔFMQ, in (**b**), the $\log(S^{6+}/S^{2-})$ vs $\log(Fe^{3+}/Fe^{2+})$ for all experiments. The gray box in both (**a**) and (**b**) shows the fO_2 range of sulfide-sulfate transition (ΔFMQ+1 to ΔFMQ+2); only the points inside the box were included in the regressions (see text

for discussion and Table 7). Black line has a slope of 2 in (**a**) and of 8 in (**b**), which are the ideal slopes predicted by thermodynamics for the sulfide-sulfate transition (Eq. 3) and the relationship between S and Fe oxidation states (Eq. 4) as a function of fO_2, respectively. Data plotted are the results of scan 1 at the intermediate level, the merged results of all scans from the highest level, and the merged results of the first ≤ 20 fly-scans from the lowest level. Dotted red and yellow lines are linear regressions through the highest and lowest level points, respectively, and the dashed blue lines are linear regressions through scan 1 points at the intermediate level. Text above or below each line is the slope of that line.

Figure 14. The $S^{6+}/\Sigma S$ estimated from scan 1 at the intermediate level and first ≤ 20 scans at the lowest level vs ΔFMQ. Black line represents the non-linear least squares fit to the data; see Table 8 for all model estimates. Colored boxes show the fO_2 of various arc-derived magmas estimated from mineral equilibria from Matthews et al. (1994) and Evans and Scaillet (1997).

Figure 1

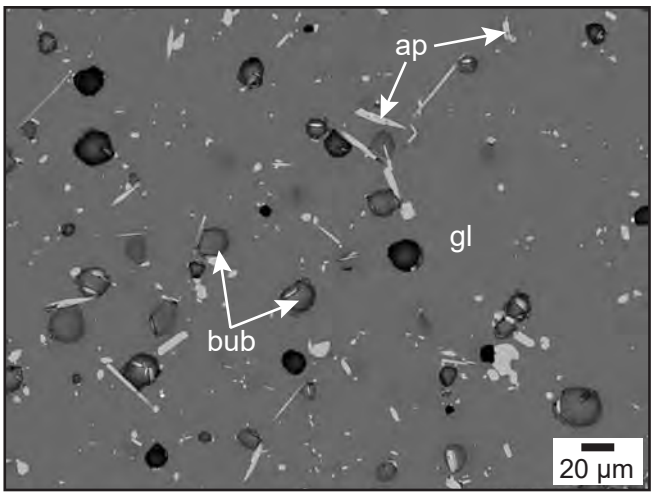

Figure 2

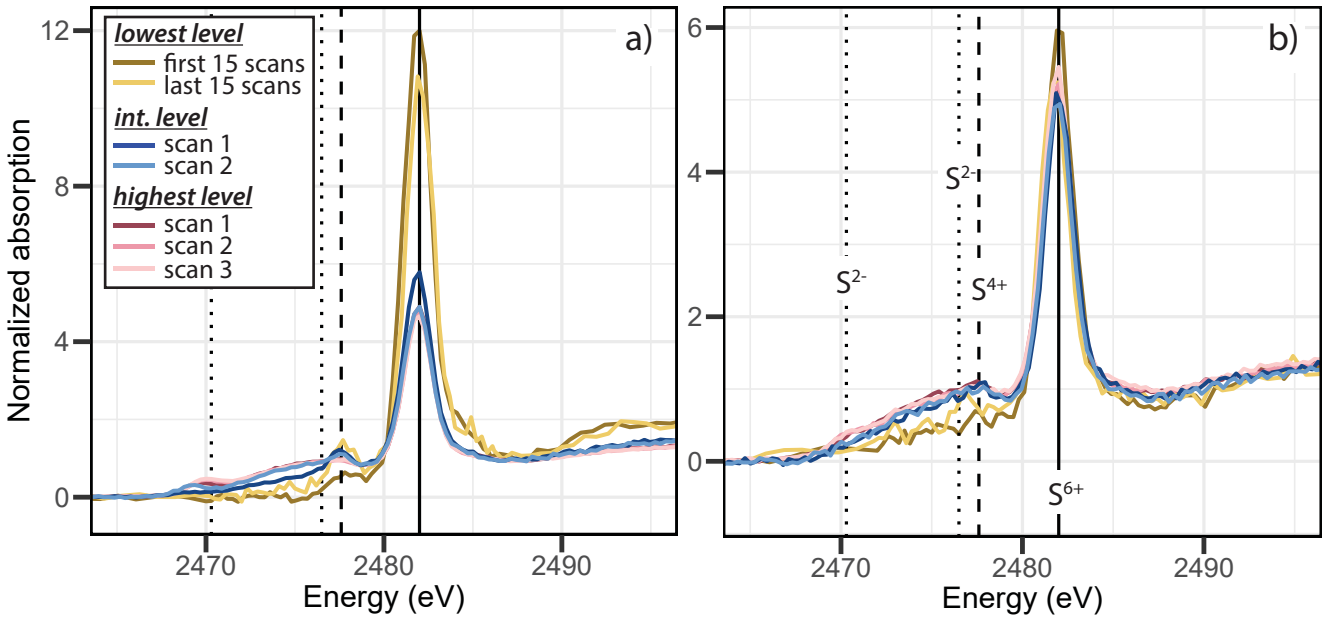

Figure 3

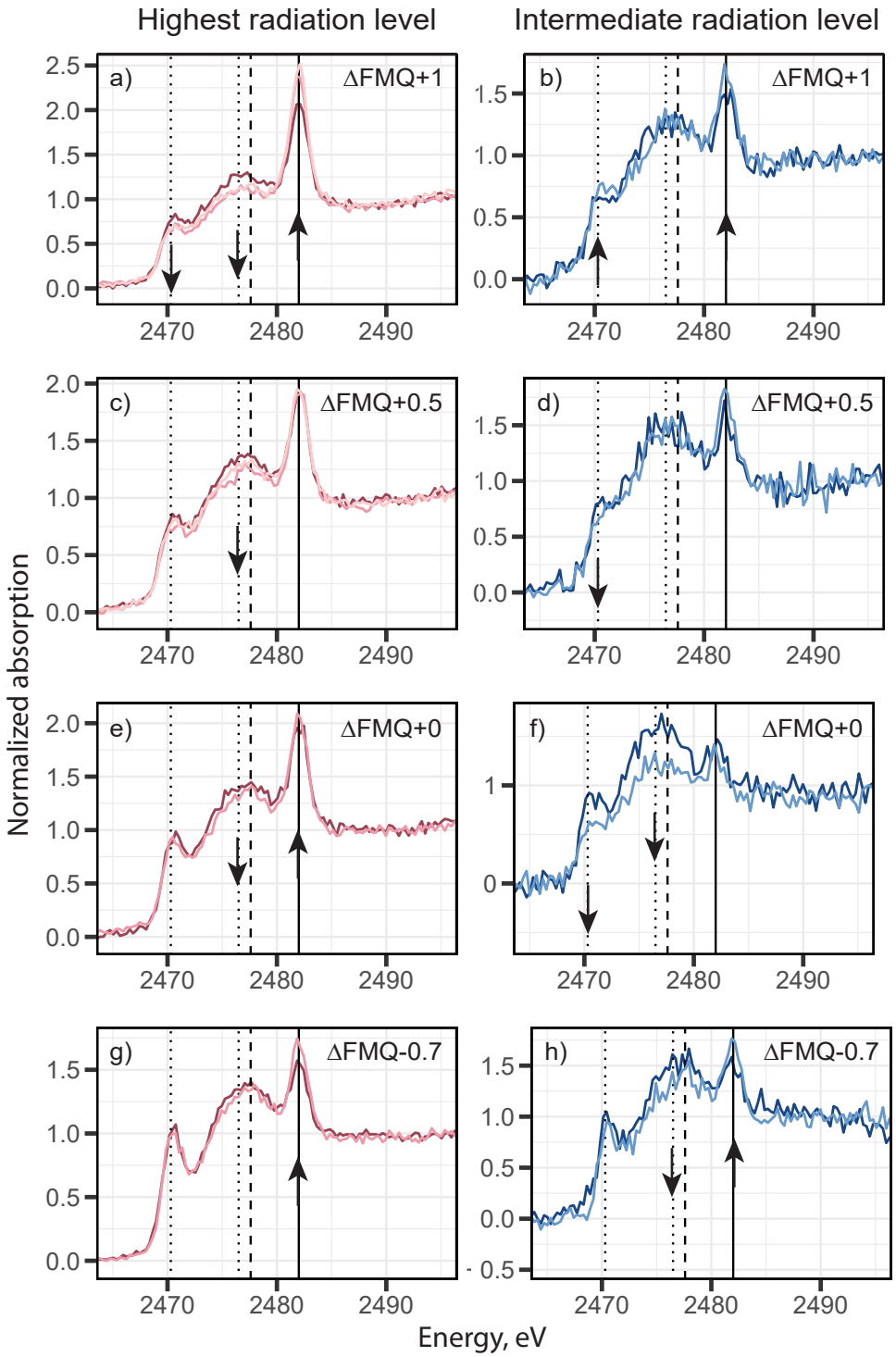
Highest radiation level
Intermediate radiation level
a)
ΔFMQ+1
b)
ΔFMQ+1
c)
ΔFMQ+0.5
d)
ΔFMQ+0.5
e)
ΔFMQ+0
f)
ΔFMQ+0
g)
ΔFMQ-0.7
h)
ΔFMQ-0.7
Normalized absorption
Energy, eV
2470
2480
2490

Figure 4

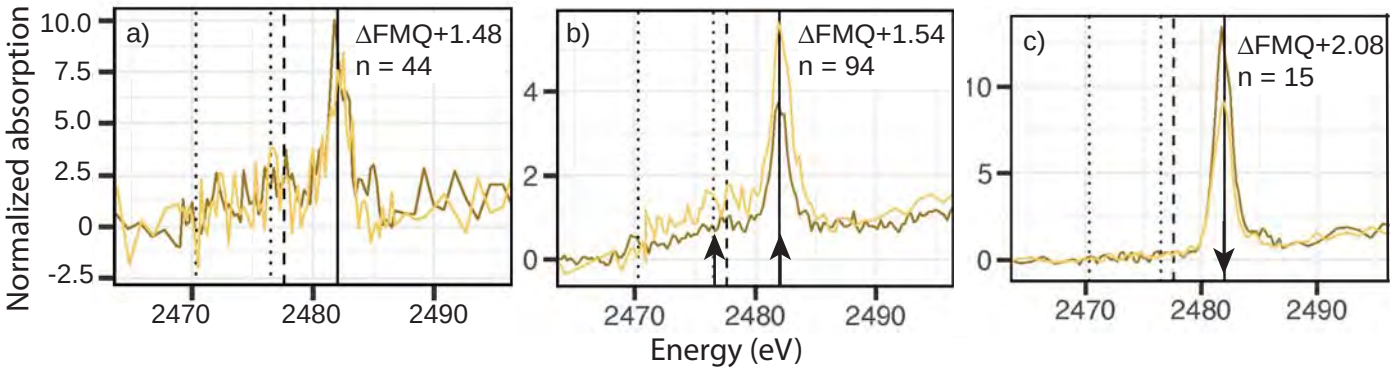

Figure 5

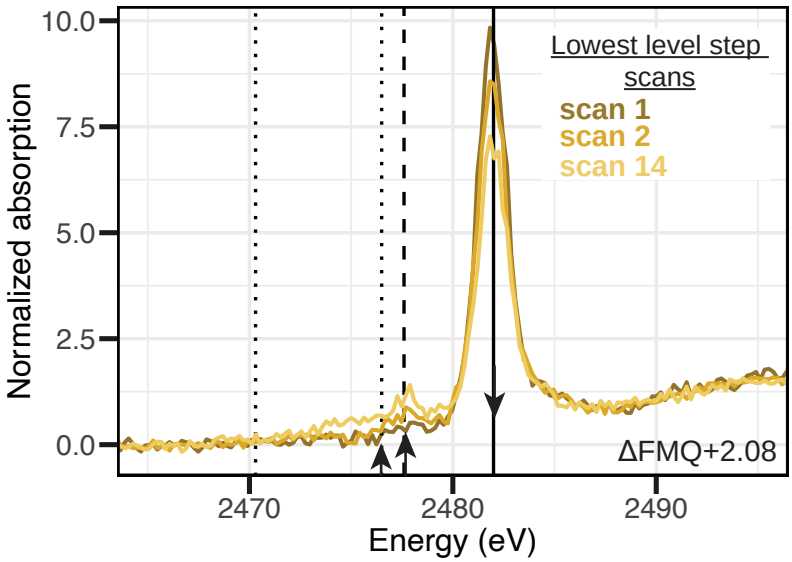

Figure 6

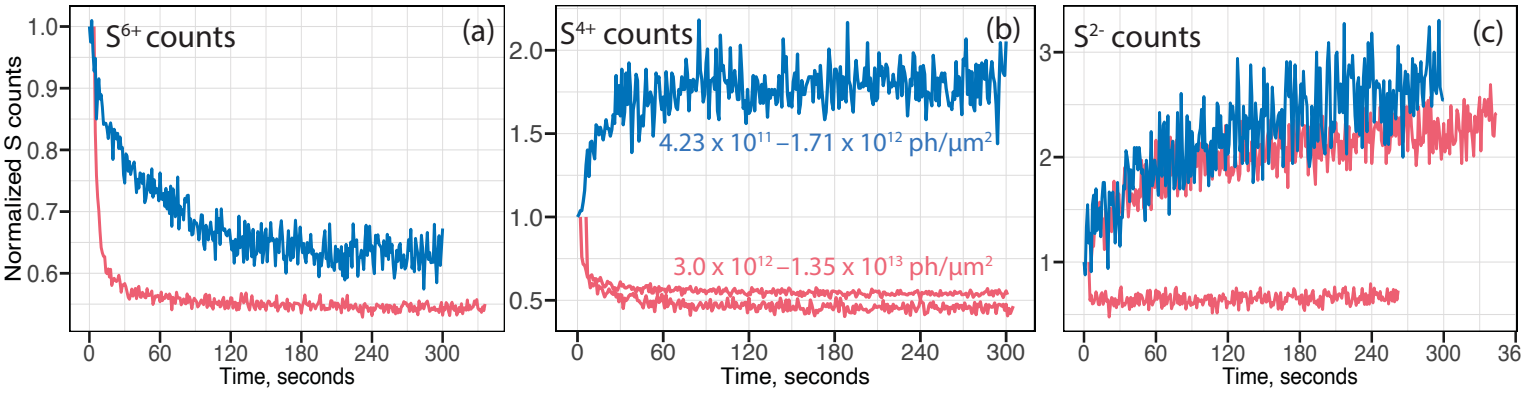

Figure 7

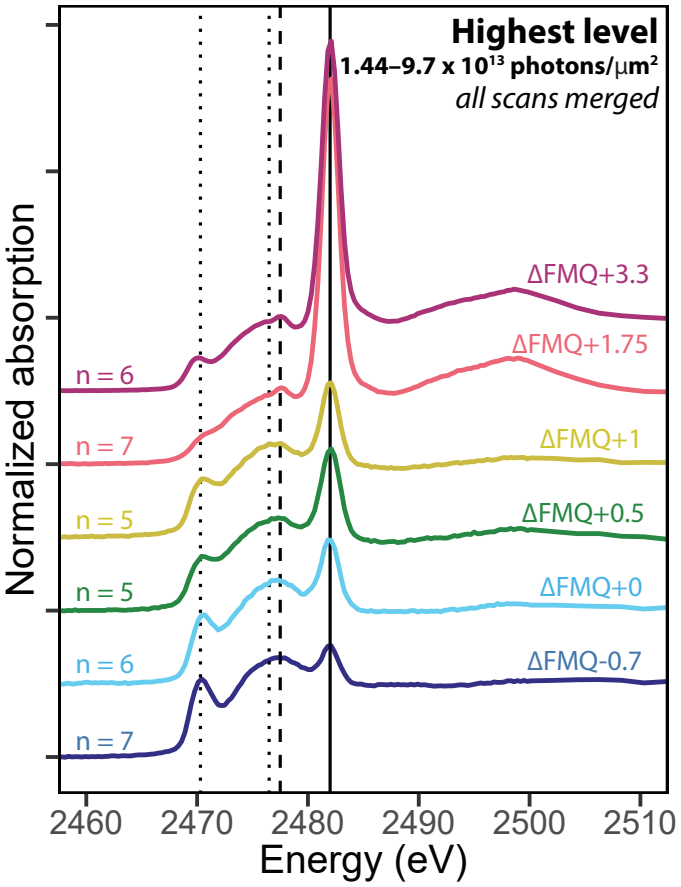

Figure 8

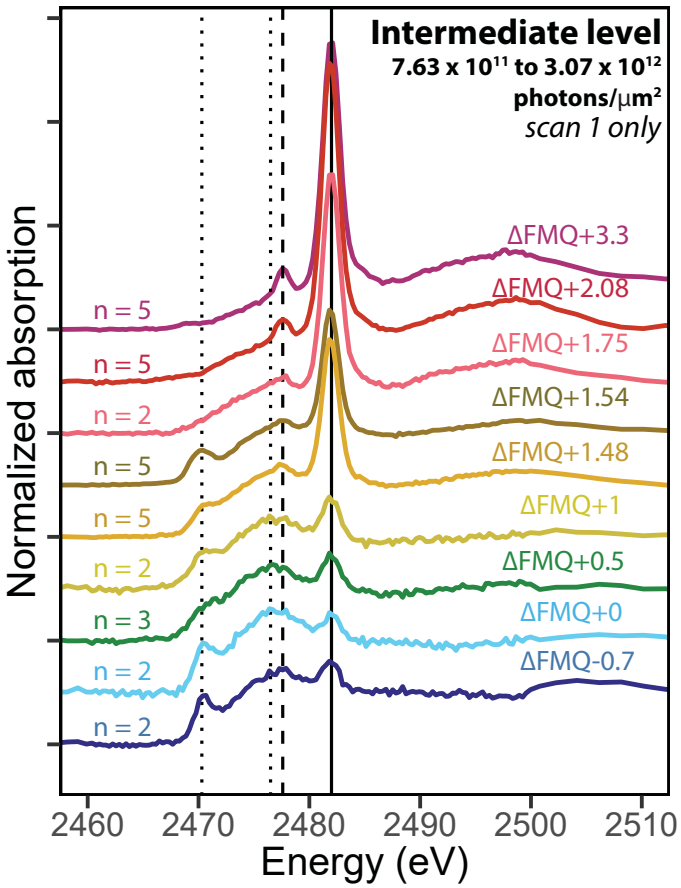

Figure 9

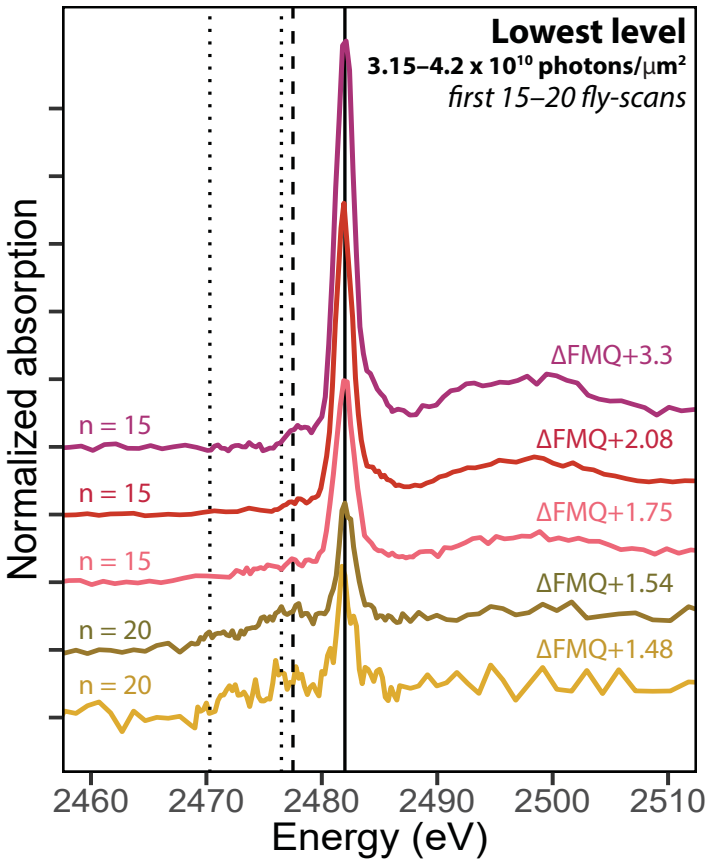

Figure 10

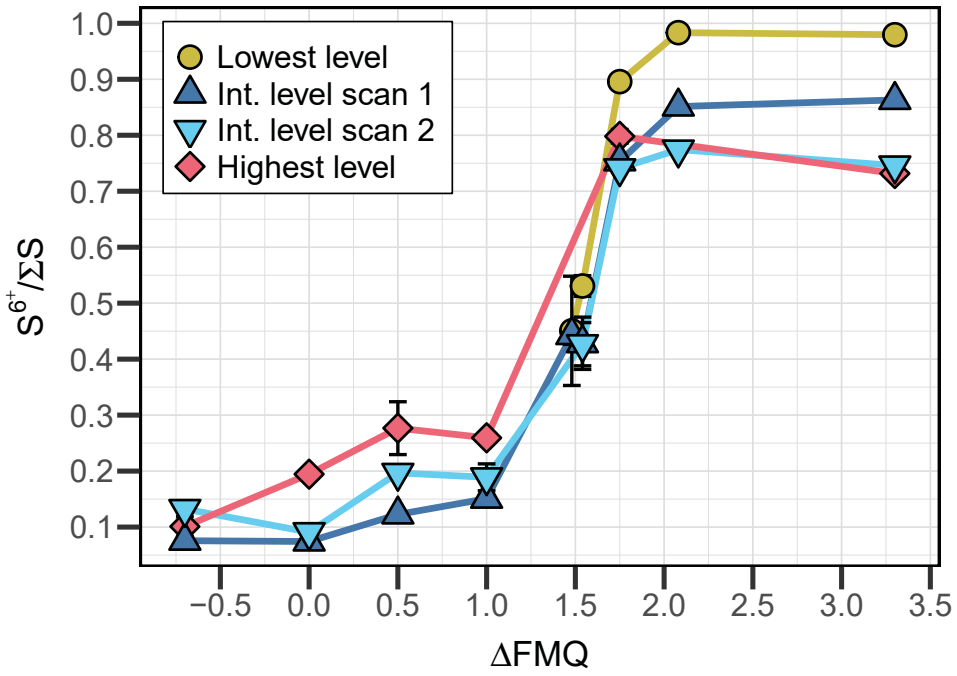

Figure 11

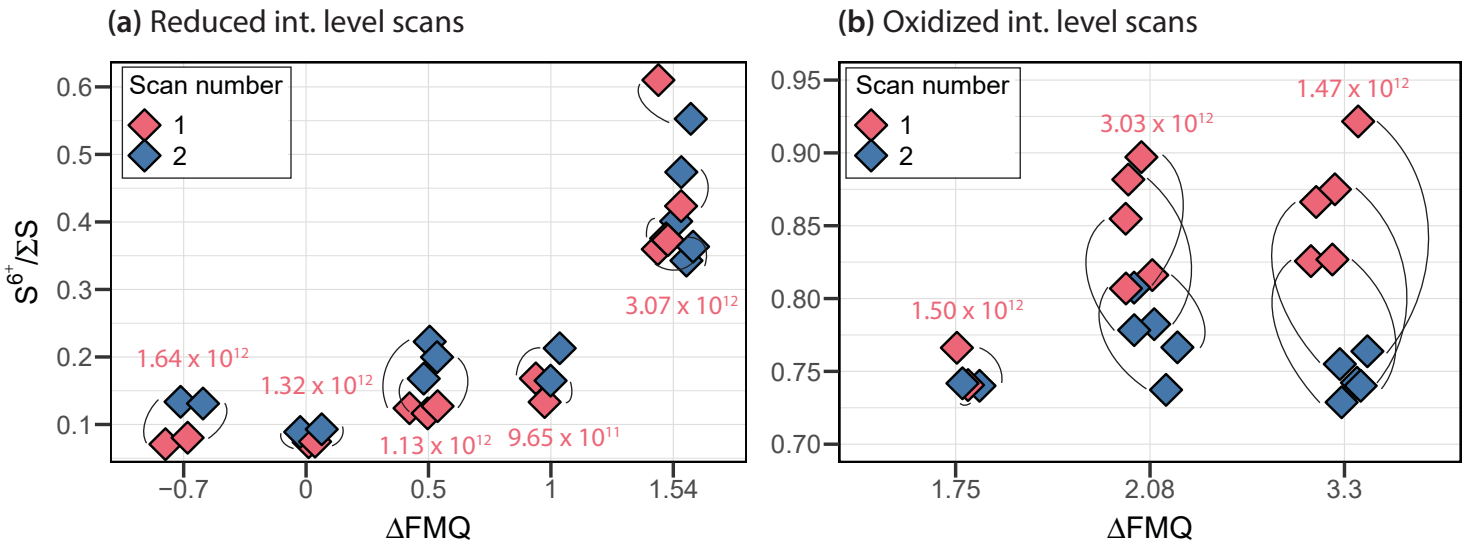

Figure 12

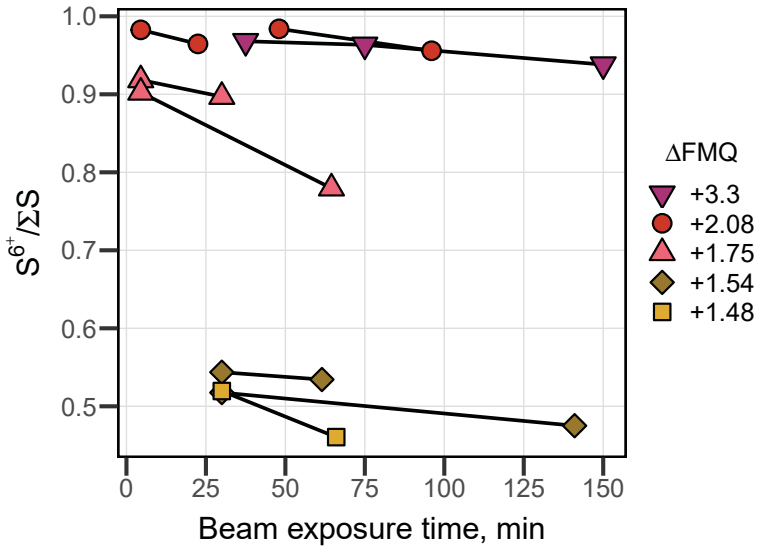

Figure 13

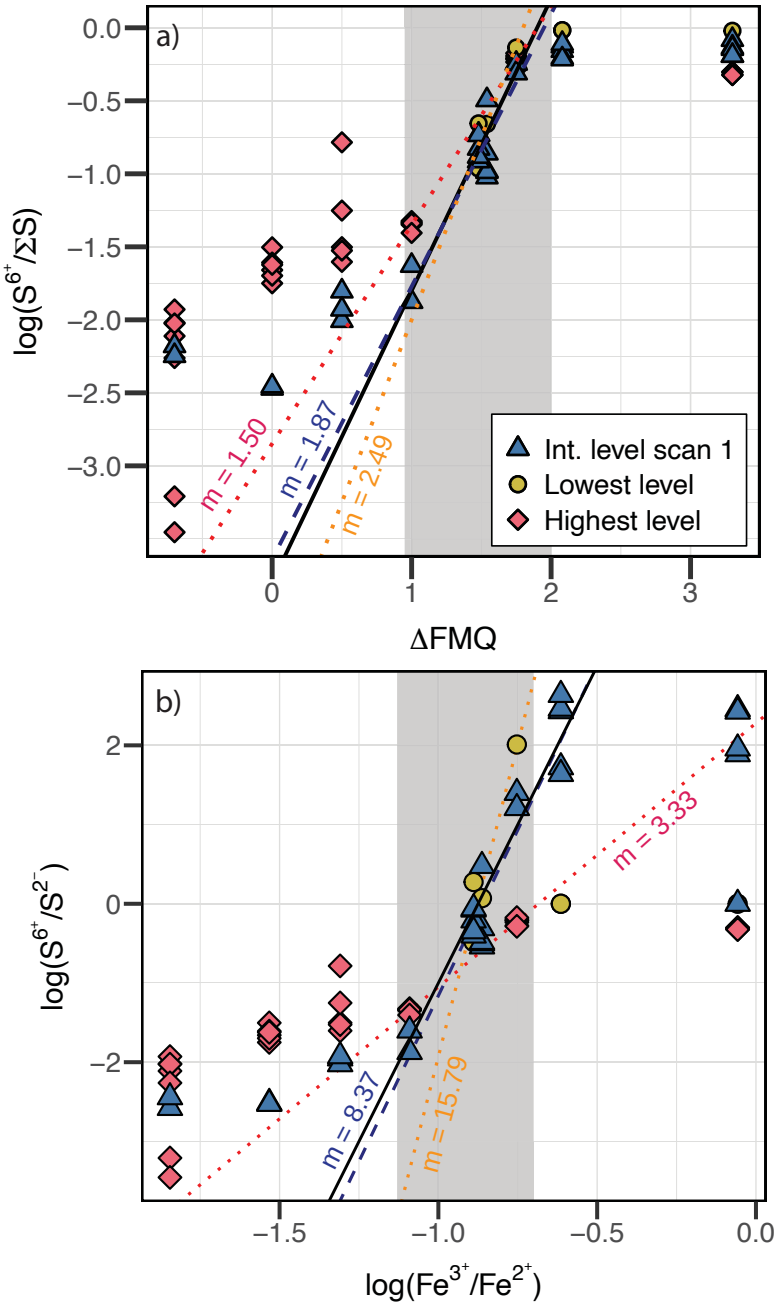

Figure 14